MULTISCALE ALGORITHMS AND COMPUTATIONS FOR THE TIME-DEPENDENT MAXWELL–SCHRÖDINGER SYSTEM IN HETEROGENEOUS NANOSTRUCTURES*

CHUPENG MA†, LIQUN CAO‡, AND YANPING LIN§

Abstract. In this paper, we discuss the multiscale computations of the time-dependent Maxwell–Schrödinger system with rapidly oscillating discontinuous coefficients. The multiscale asymptotic method for the system is presented. We propose a novel multiscale asymptotic expansion for the vector potential to capture the oscillations caused by the quantum current density. To solve the homogenized Maxwell–Schrödinger system, we present an alternating Crank–Nicolson finite element method. The stability estimates and the solvability of the discrete system are established. An iteration algorithm together with its convergence analysis is given. Numerical examples are carried out to demonstrate the efficiency and accuracy of the multiscale algorithms.

Key words. Maxwell–Schrödinger system, homogenization method, multiscale asymptotic expansion, finite element method

AMS subject classifications. 65F10, 78M05

DOI. 10.1137/18M1169709

1. Introduction. Most electronic devices and optical devices in the real world are working under a complex electromagnetic environment. In the study of these devices, researchers in the past usually only considered the impact of the electromagnetic fields on the devices, i.e., on the behaviors of electrons in these devices. However, as the size of electronic and optical devices reaches the scale of a few nanometers, quantum effects become important or even dominant, and thus we cannot neglect the back coupling effects of these nanostructures on the electromagnetic fields [19, 28]. In recent years, more and more researchers have attempted to model the optical and electrical properties of nanodevices within the framework of an electromagnetic–quantum mechanics coupled model [3, 24, 33]. In particular, the Maxwell–Schrödinger system is widely used since Schrödinger's equation and Maxwell's equations are the fundamental equations of nonrelativistic quantum mechanics and electromagnetics, respectively.

Maxwell's equations in a linear medium can be written as

$$(1.1) \quad \begin{aligned} \nabla \times \mathbf{E} + \frac{\partial \mathbf{B}}{\partial t} &= 0, & \nabla \cdot \mathbf{B} &= 0, \\ \nabla \times (\mu^{-1}\mathbf{B}) - \epsilon\frac{\partial \mathbf{E}}{\partial t} &= \mathbf{J}, & \nabla \cdot (\epsilon\mathbf{E}) &= \rho, \end{aligned}$$

†Institute of Computational Mathematics and Scientific/Engineering Computing, Academy of Mathematics and Systems Science, Chinese Academy of Sciences, Beijing 100190, China (machupeng @lsec.cc.ac.cn).

‡Corresponding author. Institute of Computational Mathematics and Scientific/Engineering Computing, Academy of Mathematics and Systems Science, Chinese Academy of Sciences, Beijing 100190, China, and School of Mathematical Sciences, University of Chinese Academy of Sciences, Beijing 100049, China (clq@lsec.cc.ac.cn).

§Department of Applied Mathematics, The Hong Kong Polytechnic University, Kowloon, Hong Kong, China (malin@polyu.edu.hk).

where $\mathbf{E}$, $\mathbf{B}$, $\mathbf{J}$, and ρ denote the electric fields, the magnetic fields, the current density, and the charge density, respectively. $\epsilon = (\epsilon_{ij})$ and $\mu = (\mu_{ij})$ are the electric permittivity and magnetic permeability, respectively.

In general, the electric fields $\mathbf{E}$ and the magnetic fields $\mathbf{B}$ can be given by the vector potential $\mathbf{A}$ and the scalar potential ϕ as follows:

$$(1.2) \qquad \mathbf{E} = -\nabla\phi - \frac{\partial \mathbf{A}}{\partial t}, \quad \mathbf{B} = \nabla \times \mathbf{A}.$$

Using $\mathbf{A}$ and ϕ, Maxwell's equations are rewritten as

$$(1.3) \qquad \begin{aligned} &\epsilon\frac{\partial^2 \mathbf{A}}{\partial t^2} + \nabla \times (\mu^{-1}\nabla \times \mathbf{A}) + \epsilon\frac{\partial(\nabla\phi)}{\partial t} = \mathbf{J}, \\ &-\nabla \cdot (\epsilon\nabla\phi) - \nabla \cdot \left(\epsilon\frac{\partial \mathbf{A}}{\partial t}\right) = \rho. \end{aligned}$$

In the presence of electromagnetic fields, Schrödinger's equation for an electron is written as [16]

$$(1.4) \qquad i\hbar\frac{\partial\Psi(\mathbf{x},t)}{\partial t} = \left\{\frac{1}{2m}(-i\hbar\nabla - q\mathbf{A})^2 + q\phi + V_c\right\}\Psi(\mathbf{x},t),$$

where $\hbar$ is the reduced Planck's constant, Ψ is the wave function, V_c is the confinement potential, m and q respectively denote the effective mass and the charge of the electron, and $\mathbf{A}$ and ϕ respectively are the vector potential and the scalar potential given in (1.3).

The quantum charge and current density of the electron are given as

$$(1.5) \qquad \rho = q|\Psi|^2, \quad \mathbf{J} = \frac{q}{m}\,\mathrm{Im}\big[\Psi^*(\hbar\nabla - iq\mathbf{A})\Psi\big],$$

where Ψ^* denotes the complex conjugate of Ψ. They satisfy the continuity equation

$$(1.6) \qquad \frac{\partial\rho}{\partial t} + \nabla \cdot \mathbf{J} = 0.$$

Combining (1.3)–(1.5), we have the Maxwell–Schrödinger coupled system

$$(1.7) \qquad \begin{cases} i\hbar\dfrac{\partial\Psi}{\partial t} = \left\{\dfrac{1}{2m}(-i\hbar\nabla - q\mathbf{A})^2 + q\phi + V_c\right\}\Psi & \text{in } \Omega \times (0,T), \\[2mm] \epsilon\dfrac{\partial^2 \mathbf{A}}{\partial t^2} + \nabla \times (\mu^{-1}\nabla \times \mathbf{A}) + \epsilon\dfrac{\partial(\nabla\phi)}{\partial t} = \mathbf{J}_s + \mathbf{J} & \text{in } \Omega \times (0,T), \\[2mm] -\nabla \cdot (\epsilon\nabla\phi) - \nabla \cdot \left(\epsilon\dfrac{\partial \mathbf{A}}{\partial t}\right) = \rho_s + \rho & \text{in } \Omega \times (0,T), \\[2mm] \rho = q|\Psi|^2, \quad \mathbf{J} = \dfrac{q}{m}\,\mathrm{Im}\big[\Psi^*(\hbar\nabla - iq\mathbf{A})\Psi\big], \end{cases}$$

where ρ_s and $\mathbf{J}_s$ are respectively the given charge and current sources satisfying a continuity equation similar to (1.6).

It is important to point out that the equation of Gauss's law in (1.7), i.e.,

$$(1.8) \qquad -\nabla \cdot (\epsilon\nabla\phi) - \nabla \cdot \left(\epsilon\frac{\partial \mathbf{A}}{\partial t}\right) = \rho_s + \rho,$$

is not an independent equation. In fact, it can be derived by taking the divergence of the second equation of (1.7) and using the continuity equation (1.6) and the consistent initial conditions. Due to this, the Maxwell–Schrödinger system (1.7) has an

intrinsic gauge freedom. If $(\Psi, \mathbf{A}, \phi)$ satisfies (1.7), then for any smooth function $\chi : \Omega \times (0, T) \to \mathbb{R}$, $(\Psi', \mathbf{A}', \phi') = (e^{\mathrm{i}q\chi}\Psi, \mathbf{A} + \nabla\chi, \phi - \frac{\partial\chi}{\partial t})$ also satisfies the system. To eliminate this gauge freedom, an additional condition for the scalar and vector potentials, known as gauge choice, is usually imposed on the solutions of the Maxwell–Schrödinger system. The most commonly used gauge choices listed below are, from left to right, the *Lorentz*, *Coulomb*, and *temporal* gauges,

$$(1.9) \qquad \nabla \cdot (\epsilon\mathbf{A}) + \frac{\partial\phi}{\partial t} = 0, \quad \nabla \cdot (\epsilon\mathbf{A}) = 0, \quad \phi = 0,$$

under which (1.8) is respectively transformed as

$$(1.10) \quad \frac{\partial^2\phi}{\partial t^2} - \nabla \cdot (\epsilon\nabla\phi) = \rho_s + \rho, \quad -\nabla \cdot (\epsilon\nabla\phi) = \rho_s + \rho, \quad -\nabla \cdot \left(\epsilon\frac{\partial\mathbf{A}}{\partial t}\right) = \rho_s + \rho.$$

The Maxwell–Schrödinger system under the Lorentz gauge and the temporal gauge is a nonlinear hyperbolic system, whereas under the Coulomb gauge it is a nonlinear hyperbolic-elliptic coupled system. The scalar potential under the temporal gauge vanishes and (1.8) can be viewed as a constraint of the Maxwell–Schrödinger system.

In this paper, we take the temporal gauge and use the atomic units, i.e., $\hbar = q = 1$. In view of the heterogeneity of practical nanostructures, we consider the following Maxwell–Schrödinger system with the rapidly oscillating effective mass and magnetic permeability:

(1.11)
$$\begin{cases} \mathrm{i}\dfrac{\partial\Psi^\varepsilon}{\partial t} = -(\nabla - \mathrm{i}\mathbf{A}^\varepsilon)\left(H\left(\dfrac{\mathbf{x}}{\varepsilon}\right)(\nabla - \mathrm{i}\mathbf{A}^\varepsilon)\right)\Psi^\varepsilon + \left(V_c\left(\dfrac{\mathbf{x}}{\varepsilon}\right) + V_{xc}(\rho^\varepsilon)\right)\Psi^\varepsilon \text{ in } \Omega \times (0, T), \\[2mm] \epsilon\dfrac{\partial^2\mathbf{A}^\varepsilon}{\partial t^2} + \nabla \times \left(B\left(\dfrac{\mathbf{x}}{\varepsilon}\right)\nabla \times \mathbf{A}^\varepsilon\right) = \mathbf{J}_s + \mathbf{J}^\varepsilon \text{ in } \Omega \times (0, T), \\[2mm] \rho^\varepsilon = N|\Psi^\varepsilon|^2, \quad \mathbf{J}^\varepsilon = 2NH\left(\dfrac{\mathbf{x}}{\varepsilon}\right)\mathrm{Im}\big[(\Psi^\varepsilon)^*(\nabla - \mathrm{i}\mathbf{A}^\varepsilon)\Psi^\varepsilon\big], \\[2mm] \Psi^\varepsilon(\mathbf{x}, t) = 0, \quad \mathbf{A}^\varepsilon(\mathbf{x}, t) \times \mathbf{n} = 0, \quad (\mathbf{x}, t) \in \partial\Omega \times (0, T), \\[2mm] \Psi^\varepsilon(\mathbf{x}, 0) = \Psi_0(\mathbf{x}), \quad \mathbf{A}^\varepsilon(\mathbf{x}, 0) = \mathbf{A}_0(\mathbf{x}), \quad \mathbf{A}_t^\varepsilon(\mathbf{x}, 0) = \mathbf{A}_1(\mathbf{x}) \text{ in } \Omega, \end{cases}$$

where N is the number of the electrons in the conduction band and $V_{xc}(\rho^\varepsilon)$ is the exchange-correlation potential function. $\Omega \subset \mathbb{R}^3$ is a bounded Lipschitz polygonal domain with a periodic microstructure occupied by a heterogeneous quantum device. Figure 1.1(a) is an illustration of a quantum device with a great number of quantum dots which are artificial semiconductor nanostructures that confine the motion of conduction band electrons [14]. $\varepsilon > 0$ is the relative size of a periodic cell for the quantum device, i.e., $0 < \varepsilon = l_p/L < 1$, where l_p and L are the sizes of a periodic cell and the device, respectively. $H(\frac{\mathbf{x}}{\varepsilon}) = (h_{ij}(\frac{\mathbf{x}}{\varepsilon}))_{3\times3}$ and $B(\frac{\mathbf{x}}{\varepsilon}) = (b_{ij}(\frac{\mathbf{x}}{\varepsilon}))_{3\times3}$ are the inverses of the effective mass and the magnetic permeability of the material, respectively.

Remark 1.1. In this paper, we only consider the heterogeneity in the effective mass and magnetic permeability of the material and assume that the electric permittivity is constant in the quantum device (for convenience, we let $\epsilon = 1$ in the rest of the paper). In fact, if the heterogeneity in the electric permittivity and magnetic permeability are both considered, it seems difficult to define the first-order cell function and the homogenized equations for Maxwell's equations in (1.11). The Maxwell–Schrödinger system with the rapidly oscillating electric permittivity will be investigated in our future work.
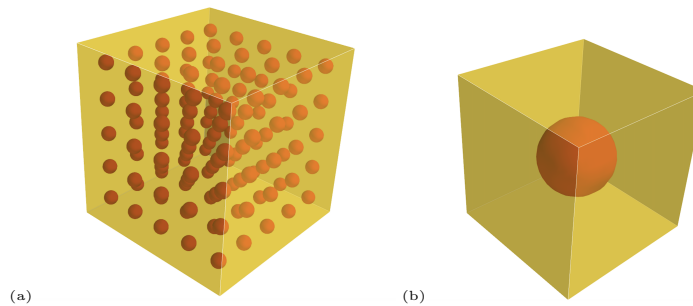
FIG. 1.1. (a) *A semiconductor device* Ω *with a great number of quantum dots;* (b) *the periodic cell Q.*

Remark 1.2. We impose the homogeneous Dirichlet boundary condition $\Psi^\varepsilon = 0$ on $\partial\Omega$ for the wave function. Physically, it implies that the electrons are confined within the quantum device. For the vector potential, we impose the perfect electric conductor boundary conditions $\mathbf{A} \times \mathbf{n} = 0$ on $\partial\Omega$. For a detailed discussion of the boundary conditions for the vector and scalar potentials, we refer the reader to [9].

In this paper, the Einstein summation convention is used: summation is taken over repeated indices. Let $\xi = \varepsilon^{-1}\mathbf{x}$. Using some notation given in section 3, we make the following assumptions:

($\mathbf{A_1}$) $h_{ij}(\xi)$, $b_{ij}(\xi)$, and $V_c(\xi)$ are rapidly oscillating 1-periodic real functions, where $h_{ij}(\xi)$ and $b_{ij}(\xi)$ are the components of $H(\xi)$ and $B(\xi)$, respectively.

($\mathbf{A_2}$) The matrices $H(\xi)$ and $B(\xi)$ are symmetric and satisfy the uniform elliptic conditions in ξ, i.e.,

$$\gamma_0|\eta|^2 \le h_{ij}(\xi)\eta_i\eta_j \le \gamma_1|\eta|^2, \quad \beta_0|\eta|^2 \le b_{ij}(\xi)\eta_i\eta_j \le \beta_1|\eta|^2, \quad |\eta|^2 = \eta_i\eta_i,$$

$$0 < \gamma_0 \le \gamma_1, \quad 0 < \beta_0 \le \beta_1, \quad \forall\eta = (\eta_1, \eta_2, \eta_3) \in \mathbb{R}^3,$$

where γ_0, γ_1, β_0, β_1 are constants independent of ε.

($\mathbf{A_3}$) h_{ij}, b_{ij} , $V_c \in L^\infty(\mathbb{R}^3)$, $\mathbf{J}_s \in C(0, T; \mathbf{L}^2(\Omega))$, $V_{xc} \in C(\mathbb{R})$.

($\mathbf{A_4}$) The initial conditions Ψ_0, $\mathbf{A}_0$, and $\mathbf{A}_1$ satisfy: $\Psi_0 \in \mathcal{H}^1(\Omega)$, $\mathbf{A}_0 \in \mathbf{H}_0(\mathbf{curl}; \Omega)$, and $\mathbf{A}_1 \in \mathbf{L}^2(\Omega)$.

Over the past decade, the Maxwell–Schrödinger system has become a popular model for the simulation of light-matter interactions in nanostructures, and numerical algorithms for this system have attracted much attention. We list some interesting studies. In [1], Ahmed and Li apply the finite-difference time-domain (FDTD) approach to solve the Maxwell–Schrödinger coupled system for the simulation of plasmonics nanodevices. In [24], Pierantoni and his collaborators simulate the interaction between the electromagnetic fields and the electrons in the carton nanotube by solving the Maxwell–Schrödinger system with the transmission line matrix (TLM) method. In [10], structure-preserving geometric algorithms are developed for numerically solving the Maxwell–Schrödinger system to model the photon-matter interactions. For other more numerical methods for the Maxwell–Schrödinger system, we refer the reader to [11, 18, 21, 22, 25, 32] and references therein.

It is worth noting that the existing studies on the Maxwell–Schrödinger system all focus on the system in a homogeneous medium. In fact, most of electronic and optical nanodevices in real-world applications are heterogeneous, and some of them

are designed with a periodic microstructure [15]. The rapidly oscillating discontinuous coefficients pose a great challenge to the numerical computations and theoretical analysis of the Maxwell–Schrödinger system in these nanostructures, especially in the cases when the relativistic size of the heterogeneities, i.e., ε in (1.11), is very small. To overcome this difficulty, the homogenization method, which gives the overall behavior of the solution by incorporating the fluctuation due to the heterogeneities, can be applied. In addition, if $\varepsilon > 0$ is not sufficiently small, the accuracy of the homogenization method may not be satisfactory. In this case one needs to resort to the multiscale asymptotic method and seek multiscale approximate solutions.

The homogenization and multiscale asymptotic method for Maxwell's equations has been studied extensively. In [4], Bensoussan, Lions, and Papanicolaou studied the homogenization method for the Maxwell-type equations with rapidly oscillating coefficients and obtained the convergence results. Wellander [30, 31] proved the convergence of the homogenization method for the time-dependent Maxwell equations in a heterogeneous medium by using the two-scale convergence method. Cao's group [6, 7, 35] developed the multiscale asymptotic method for the stationary and time-dependent Maxwell equations and obtained the explicit convergence rates. Likewise, many studies on the homogenization and multiscale methods for the Schrödinger equation with rapidly oscillating coefficients and potential have been reported [2, 8, 26, 34]. However, to the best of our knowledge, there exists little literature concerning the homogenization and multiscale asymptotic method for the Maxwell–Schrödinger coupled system in heterogeneous materials.

In this paper, we develop the homogenization and multiscale asymptotic method for the Maxwell–Schrödinger system with rapidly oscillating discontinuous coefficients. In the Maxwell–Schrödinger coupled system (1.11), the rapidly oscillating quantum current density $\mathbf{J}^\varepsilon$ plays a vital role. The (traditional) multiscale asymptotic method for Maxwell's equations fails to capture the oscillations of the vector potential $\mathbf{A}^\varepsilon$ arising from the quantum current density, making its accuracy unsatisfactory in the cases when the quantum current density causes considerable oscillations in the vector potential. To overcome this difficulty, we propose a modified multiscale asymptotic method for the vector potential and confirm its validity by numerical examples. Note that most of the multiscale asymptotic methods for PDEs in heterogeneous materials aim at capturing the oscillations of solutions caused by the discontinuous coefficients and neglect the effects of the source term. Our method might provide some insights into how to deal with the rapidly oscillating source term in the multiscale methods. Another focus of this paper is the numerical method for the homogenized Maxwell–Schrödinger system, i.e., the Maxwell–Schrödinger system with constant coefficients. We propose an alternating Crank–Nicolson finite element method for the homogenized Maxwell–Schrödinger system and establish the stability estimates. Compared to the commonly used FDTD method [1, 25, 32], this scheme has two main advantages. First, it can be applied to the Maxwell–Schrödinger system with discontinuous coefficients directly. Second, our method conserves the charge and the energy of the discrete system ($\mathbf{J}_s = 0$) and thus is more stable.

The rest of this paper is organized as follows. In section 2, we present the homogenization and multiscale asymptotic method for the Maxwell–Schrödinger system (1.11). A modified multiscale asymptotic method for the vector potential is given. In section 3, we propose the numerical algorithms for solving the cell functions and the homogenized Maxwell–Schrödinger system. In section 4, numerical examples are presented to demonstrate the validity and efficiency of our method.

2. Homogenization and multiscale asymptotic method. In this section, we present the homogenization and multiscale asymptotic method for the Maxwell–Schrödinger system (1.11). We first give the multiscale asymptotic expansions for the solution of the Maxwell–Schrödinger system. Formally, we set

(2.1)
$$\Psi^\varepsilon = \Psi^0 + \varepsilon\theta_m(\xi)\left(\frac{\partial}{\partial x_m} - i\mathbf{A}_m^0\right)\Psi^0 + \varepsilon^2\theta_{ml}(\xi)\left(\frac{\partial}{\partial x_m} - i\mathbf{A}_m^0\right)\left(\frac{\partial}{\partial x_l} - i\mathbf{A}_l^0\right)\Psi^0 + \cdots,$$
$$\mathbf{A}^\varepsilon = \mathbf{A}^0 + \varepsilon\Theta_1(\xi)\nabla \times \mathbf{A}^0 + \varepsilon^2\Theta_2(\xi)\nabla \times (\nabla \times \mathbf{A}^0) + \cdots,$$

where $\mathbf{A}_m^0$ is the mth component of $\mathbf{A}^0$, and $\theta_m(\xi)$, $\theta_{ml}(\xi)$, $\Theta_1(\xi)$, and $\Theta_2(\xi)$ are the cell functions defined below.

Remark 2.1. The formal expansions (2.1) are motivated by the multiscale asymptotic expansion

(2.2)
$$u^\varepsilon = u^0 + \chi^i(\xi)\frac{\partial u^0}{\partial x_i} + \chi^{ij}(\xi)\frac{\partial^2 u^0}{\partial x_i\partial x_j} + \cdots$$

in Chapter 1, page 12 of [4] for the Poisson equation $-\nabla(a(\frac{\mathbf{x}}{\varepsilon})\nabla u^\varepsilon) = f$ (see also Chapter 7 of [12]). In the asymptotic expansion of the vector potential $\mathbf{A}$, we replace the derivatives $\frac{\partial}{\partial x_i}$ and $\frac{\partial^2}{\partial x_i\partial x_j}$ with the curl and double curl operators, i.e., $\nabla\times$ and $\nabla \times \nabla\times$, respectively. The key step in our approach is the construction of the cell functions.

Without loss of generality, we assume that the reference cell $Q = (0,1)^3$. Next we substitute the expansions (2.1) into (1.11). Treating $\mathbf{x}$ and ξ as independent variables and using the chain rule, the operators ∇ and $\nabla\times$ in (1.11) become $\nabla_{\mathbf{x}} + \varepsilon^{-1}\nabla_\xi$ and $\nabla_{\mathbf{x}} \times +\varepsilon^{-1}\nabla_\xi\times$, respectively. By equating the coefficients of power ε^{-1} in (1.11), in a standard way (see Chapter 1, pages 12 and 139 of [4] and Chapter 7, page 125 of [12]), we can define the first-order cell functions $\theta_m(\xi)$ ($m = 1, 2, 3$) and $\Theta_1(\xi) = (\Theta_1^1(\xi), \Theta_1^2(\xi), \Theta_1^3(\xi))$ as follows:

(2.3)
$$\begin{cases} \dfrac{\partial}{\partial\xi_i}\left(h_{ij}(\xi)\dfrac{\partial\theta_m(\xi)}{\partial\xi_j}\right) = -\dfrac{\partial}{\partial\xi_i}\big(h_{im}(\xi)\big), & \xi \in Q, \\ \theta_m(\xi) \quad\text{is 1-periodic in } \xi, \\ \displaystyle\int_Q \theta_m(\xi)d\xi = 0, & m = 1, 2, 3, \end{cases}$$

and

(2.4)
$$\begin{cases} \nabla_\xi \times \big(B(\xi)\nabla_\xi \times \Theta_1^p(\xi)\big) = -\nabla_\xi \times (B(\xi)\mathbf{e}_p), & \xi \in Q, \\ \nabla_\xi \cdot \Theta_1^p(\xi) = 0, & \xi \in Q, \\ \Theta_1^p(\xi) \times \mathbf{n} = 0, & \xi \in \partial Q, \quad p = 1, 2, 3, \end{cases}$$

where $\mathbf{n}$ is the outward unit normal to ∂Q and $\mathbf{e}_1 = \{1, 0, 0\}^T, \mathbf{e}_2 = \{0, 1, 0\}^T, \mathbf{e}_3 = \{0, 0, 1\}^T$.

Next, by equating the coefficients of power ε^0 in Schrödinger's equation, we define

the second-order cell functions $\theta_{ml}(\xi)$ $(m, l = 1, 2, 3)$ as

(2.5)
$$\begin{cases} \dfrac{\partial}{\partial \xi_i}\left(h_{ij}(\xi)\dfrac{\partial \theta_{ml}(\xi)}{\partial \xi_j}\right) = -\dfrac{\partial}{\partial \xi_i}\big(h_{im}(\xi)\theta_l(\xi)\big) \\[2mm] \qquad -h_{mj}(\xi)\dfrac{\partial \theta_l(\xi)}{\partial \xi_j} - h_{ml}(\xi) + \hat{h}_{ml}, \quad \xi \in Q, \\[2mm] \theta_{ml}(\xi) \quad \text{is 1-periodic in } \xi, \\[2mm] \displaystyle\int_Q \theta_{ml}(\xi)d\xi = 0, \quad m, l = 1, 2, 3, \end{cases}$$

where $\hat{h}_{ml}$ $(m, l = 1, 2, 3)$ are the components of the homogenized coefficients matrix $\hat{H}$ for Schrödinger's equation:

(2.6) $$\hat{H} = \int_Q \big(H(\xi) + H(\xi)\nabla_\xi \boldsymbol{\theta}(\xi)\big)d\xi, \quad \boldsymbol{\theta}(\xi) = (\theta_1(\xi), \theta_2(\xi), \theta_3(\xi)), \quad Q = (0,1)^3.$$

Similarly, by equating the coefficients of power ε^0 in the Maxwell's equations and following the idea of [35], we give the second-order cell function $\Theta_2(\xi) = (\Theta_2^1(\xi), \Theta_2^2(\xi), \Theta_2^3(\xi))$ by
(2.7)
$$\begin{cases} \nabla_\xi \times \big(B(\xi)\nabla_\xi \times \Theta_2^p(\xi)\big) = -\nabla_\xi \times (B(\xi)\Theta_1^p(\xi)) + G^p(\xi) + \nabla_\xi \varphi^p(\xi), \quad \xi \in Q, \\[2mm] \nabla_\xi \cdot \Theta_2^p(\xi) = 0, \quad \xi \in Q, \\[2mm] \Theta_2^p(\xi) \times \mathbf{n} = 0, \quad \xi \in \partial Q, \quad p = 1, 2, 3, \end{cases}$$

where $G^p(\xi) = -B(\xi)\nabla_\xi \times \Theta_1^p(\xi) - B(\xi)\mathbf{e}_p + \hat{B}\mathbf{e}_p$ with $\hat{B}$ being the homogenized coefficients matrix for Maxwell's equations

(2.8) $$\hat{B} = \int_Q \big(B(\xi) + B(\xi)\nabla_\xi \times \Theta_1(\xi)\big)d\xi, \quad Q = (0,1)^3,$$

and $\varphi^p(\xi)$ $(p = 1, 2, 3)$ are given by

(2.9) $$\begin{cases} -\Delta_\xi \varphi^p(\xi) = \nabla_\xi \cdot G^p(\xi), \ \xi \in Q, \\ \varphi^p(\xi) = 0, \ \xi \in \partial Q, \quad p = 1, 2, 3. \end{cases}$$

Remark 2.2. If the heterogeneity in the electric permittivity is considered in (1.11), it is difficult to define the first-order cell functions (2.4) and the homogenized coefficient (2.8) for Maxwell's equations.

Remark 2.3. Existence and uniqueness of solutions to the cell problems (2.3)–(2.5) and (2.7) can be proved by using the assumptions $(\mathbf{A_1})$–$(\mathbf{A_3})$ in section 1 and the (generalized) Lax–Milgram theorem in Chapter 2 of [23]. In addition, under the assumption $(\mathbf{A_2})$, the homogenized matrices $\hat{H}$ and $\hat{B}$ are symmetric and positive definite (see Chapter 1 of [4]).

Following the line of reasoning in Chapter 7, page 130, of [12] (see also Chapter 1 of [4]), we have the following homogenized Maxwell–Schrödinger system associated

to (1.11):

(2.10)
$$
\begin{cases}
i\dfrac{\partial \Psi^0}{\partial t} = -(\nabla - i\mathbf{A}^0)\big(\hat{H}\,(\nabla - i\mathbf{A}^0)\Psi^0\big) + \big(\langle V_c\rangle + V_{xc}(\rho^0)\big)\Psi^0 \quad \text{in } \Omega \times (0,T), \\[2mm]
\dfrac{\partial^2 \mathbf{A}^0}{\partial t^2} + \nabla \times (\hat{B}\,\nabla \times \mathbf{A}^0) = \mathbf{J}_s + \mathbf{J}^0 \quad \text{in } \Omega \times (0,T), \\[2mm]
\rho^0 = N|\Psi^0|^2, \quad \mathbf{J}^0 = 2N\hat{H}\,\mathrm{Im}\big[(\Psi^0)^*(\nabla - i\mathbf{A}^0)\Psi^0\big], \\[2mm]
\Psi^0(\mathbf{x},t) = 0, \quad \mathbf{A}^0(\mathbf{x},t) \times \mathbf{n} = 0, \quad (\mathbf{x},t) \in \partial\Omega \times (0,T), \\[2mm]
\Psi^0(\mathbf{x},0) = \Psi_0(\mathbf{x}), \quad \mathbf{A}^0(\mathbf{x},0) = \mathbf{A}_0(\mathbf{x}), \quad \mathbf{A}_t^0(\mathbf{x},0) = \mathbf{A}_1(\mathbf{x}) \text{ in } \Omega,
\end{cases}
$$

where $\langle V_c\rangle = \int_Q V_c(\xi)d\xi$, and $\hat{H}$ and $\hat{B}$ are given by (2.6) and (2.8), respectively.

Remark 2.4. The homogenized Maxwell–Schrödinger system (2.10) is obtained by a formal computation. A rigorous proof of the convergence of $(\Psi^\varepsilon, \mathbf{A}^\varepsilon)_\varepsilon$ to $(\Psi^0, \mathbf{A}^0)$ in a suitable sense is challenging for two main reasons. First, as of now, the existence, uniqueness, and regularity of solutions to the Maxwell–Schrödinger system (1.11) in a bounded domain are still an open problem. Second, a common and natural regularity assumption of $(\Psi^\varepsilon, \mathbf{A}^\varepsilon)_\varepsilon$, for example,

(2.11)
$$
\|\Psi^\varepsilon\|_{L^\infty(0,T;H^1(\Omega))} + \|\mathbf{A}^\varepsilon\|_{L^\infty(0,T;\mathbf{H}(\mathbf{curl};\Omega))} \leq C \quad \forall \varepsilon,
$$

seems insufficient for bounding the nonlinear terms in the convergence proof.

The first-order and second-order multiscale approximate solutions of (1.11) are given by

(2.12)
$$
\begin{aligned}
\Psi_1^\varepsilon(\mathbf{x},t) &= \Psi^0(\mathbf{x},t) + \varepsilon\theta_m(\xi)\bigg(\frac{\partial}{\partial x_m} - i\mathbf{A}_m^0\bigg)\Psi^0(\mathbf{x},t), \\
\mathbf{A}_1^\varepsilon(\mathbf{x},t) &= \mathbf{A}^0(\mathbf{x},t) + \varepsilon\Theta_1(\xi)\nabla \times \mathbf{A}^0(\mathbf{x},t)
\end{aligned}
$$

and

(2.13)
$$
\begin{aligned}
\Psi_2^\varepsilon(\mathbf{x},t) &= \Psi_1^\varepsilon(\mathbf{x},t) + \varepsilon^2\theta_{ml}(\xi)\bigg(\frac{\partial}{\partial x_m} - i\mathbf{A}_m^0\bigg)\bigg(\frac{\partial}{\partial x_l} - i\mathbf{A}_l^0\bigg)\Psi^0(\mathbf{x},t), \\
\mathbf{A}_2^\varepsilon(\mathbf{x},t) &= \mathbf{A}_1^\varepsilon(\mathbf{x},t) + \varepsilon^2\Theta_2(\xi)\nabla \times (\nabla \times \mathbf{A}^0(\mathbf{x},t)).
\end{aligned}
$$

Numerical results presented in section 4 show that the multiscale approximation solutions defined in (2.12)–(2.13) fail to capture the oscillations of the vector potential caused by the quantum current density and thus produce the inaccurate results in the region where the vector potential is greatly affected by the quantum current density. As we can see from the equation

(2.14)
$$
\frac{\partial^2 \mathbf{A}^\varepsilon}{\partial t^2} + \nabla \times \bigg(B\bigg(\frac{\mathbf{x}}{\varepsilon}\bigg)\nabla \times \mathbf{A}^\varepsilon\bigg) = \mathbf{J}_s + \mathbf{J}^\varepsilon,
$$

the oscillations of the vector potential $\mathbf{A}^\varepsilon$ mainly arise from the discontinuous coefficients matrix $B(\frac{\mathbf{x}}{\varepsilon})$ and the rapidly oscillating quantum current density $\mathbf{J}^\varepsilon$. In the (traditional) multiscale asymptotic method, in order to capture the oscillations of the vector potential $\mathbf{A}^\varepsilon$ caused by $B(\frac{\mathbf{x}}{\varepsilon})$, the first-order corrector and the second-order corrector via the cell functions $\Theta_1(\xi)$ and $\Theta_2(\xi)$ are defined. However, for the quantum current density $\mathbf{J}^\varepsilon$, in the asymptotic expansions we simply replace it with its integral average value over the reference cell Q. This may be reasonable if $\varepsilon \to 0$ or

the oscillation characteristic of $\mathbf{J}^\varepsilon$, which depends on the coefficient matrix $H(\frac{\mathbf{x}}{\varepsilon})$ and the number of the electrons N, can be neglected. However, if ε is not sufficiently small and the oscillations of $\mathbf{A}^\varepsilon$ caused by $\mathbf{J}^\varepsilon$ are comparable to those caused by $B(\frac{\mathbf{x}}{\varepsilon})$, the multiscale solutions $\mathbf{A}_1^\varepsilon$ and $\mathbf{A}_2^\varepsilon$ may not be good approximations of $\mathbf{A}^\varepsilon$.

Taking what we have discussed above into consideration, we present the following modified multiscale approximate solution for the vector potential $\mathbf{A}^\varepsilon$:

(2.15)
$$\tilde{\mathbf{A}}^\varepsilon(\mathbf{x}, t) = (\mathrm{I} + \mathrm{M}(\xi, t)\rho^0)\mathbf{A}^0 + \varepsilon\Theta_1(\xi)\nabla \times \mathbf{A}^0(\mathbf{x}, t) + \varepsilon^2\Theta_2(\xi)\nabla \times (\nabla \times \mathbf{A}^0(\mathbf{x}, t)),$$

where ρ^0 is the quantum charge density, I is the unit matrix, and $\mathrm{M}(\xi, t)$ is the time-dependent matrix-value cell function to be determined.

Remark 2.5. The modified multiscale solution $\tilde{\mathbf{A}}^\varepsilon$ is given by adding a new term $\mathrm{M}(\xi, t)\rho^0\mathbf{A}^0$ to the second-order multiscale solution $\mathbf{A}_2^\varepsilon$. The quantum charge density ρ^0 in (2.15) acts as a weight function. It is introduced based on the consideration that the original multiscale solutions $\mathbf{A}^{\varepsilon,1}$ and $\mathbf{A}^{\varepsilon,2}$ should be mainly modified in the domain where the quantum current density rapidly oscillates, which in general coincides with the domain where the quantum charge density is concentrated.

Substituting (2.15) into (2.14) and recalling the definitions of cell functions $\Theta_1(\xi)$ and $\Theta_2(\xi)$, we have

(2.16)
$$\varepsilon^{-2}\nabla_\xi \times (B(\xi)\nabla_\xi \times \mathrm{M}(\xi, t))\rho^0\mathbf{A}^0 + \varepsilon^{-1}\nabla_\xi \times (B(\xi)\mathrm{M}(\xi, t))\nabla_\mathbf{x} \times (\rho^0\mathbf{A}^0)$$
$$+ \varepsilon^{-1}B(\xi)\nabla_\xi \times \mathrm{M}(\xi, t)\nabla_\mathbf{x} \times (\rho^0\mathbf{A}^0) + B(\xi)\mathrm{M}(\xi, t)\nabla_\mathbf{x} \times (\nabla_\mathbf{x} \times (\rho^0\mathbf{A}^0))$$
$$+ \frac{\partial^2(\mathrm{M}(\xi, t)\rho^0\mathbf{A}^0)}{\partial t^2} = 2N(H(\xi) + H(\xi)\nabla_\xi\boldsymbol{\theta}(\xi) - \hat{H})\,\mathrm{Im}\big[(\Psi^0)^*(\nabla_\mathbf{x} - \mathrm{i}\mathbf{A}^0)\Psi^0\big],$$

where we have dropped the terms with ε^s ($s \geq 1$) and $\boldsymbol{\theta}(\xi)$ is given in (2.6). Next we integrate (2.16) over the whole domain Ω. By using integration by parts and the fact that ρ^0 and $\nabla\rho^0$ both vanish on the boundary $\partial\Omega$, we obtain

(2.17)
$$\frac{\partial^2(\mathrm{M}(\xi, t)\mathbf{f}(t))}{\partial t^2} + \varepsilon^{-2}\nabla_\xi \times (B(\xi)\nabla_\xi \times \mathrm{M}(\xi, t))\mathbf{f}(t)$$
$$= (H(\xi) + H(\xi)\nabla_\xi\boldsymbol{\theta}(\xi) - \hat{H})\int_\Omega 2N\,\mathrm{Im}\big[(\Psi^0)^*(\nabla_\mathbf{x} - \mathrm{i}\mathbf{A}^0)\Psi^0\big]d\mathbf{x},$$

where $\mathbf{f}(t) = \int_\Omega \mathbf{A}^0\rho^0\, d\mathbf{x}$. By keeping the second-order temporal and spatial derivative terms of $\mathrm{M}(\xi, t)$ and discarding all the other terms on the left-hand side of (2.17), we arrive at

(2.18)
$$\left(\frac{\partial^2\mathrm{M}(\xi, t)}{\partial t^2} + \varepsilon^{-2}\nabla_\xi \times (B(\xi)\nabla_\xi \times \mathrm{M}(\xi, t))\right)\mathbf{f}(t)$$
$$= (H(\xi) + H(\xi)\nabla_\xi\boldsymbol{\theta}(\xi) - \hat{H})\int_\Omega 2N\,\mathrm{Im}\big[(\Psi^0)^*(\nabla_\mathbf{x} - \mathrm{i}\mathbf{A}^0)\Psi^0\big]d\mathbf{x}.$$

Now we can define the new cell function $\mathrm{M}(\xi, t) = (\mathrm{M}^1(\xi, t),\ \mathrm{M}^2(\xi, t),\ \mathrm{M}^3(\xi, t))$ as follows:

(2.19)
$$\begin{cases} \dfrac{\partial^2 \mathrm{M}^j(\xi,t)}{\partial t^2} + \varepsilon^{-2}\nabla_\xi \times (B(\xi)\nabla_\xi \times \mathrm{M}^j(\xi,t)) = \big(H(\xi) + H(\xi)\nabla_\xi\boldsymbol{\theta}(\xi) - \hat{H}\big)\mathbf{e}_j\eta^j(t), \\ \qquad\qquad\qquad\qquad\qquad\qquad\qquad\qquad\qquad (\xi,t) \in Q \times (0,T), \\ \mathrm{M}^j(\xi,t) \times \mathbf{n} = 0, \quad (\xi,t) \in \partial Q \times (0,T), \\ \mathrm{M}^j(\xi,t) \quad \text{is 1-periodic in } \xi, \\ \mathrm{M}^j(\xi,0) = 0, \quad \mathrm{M}^j_t(\xi,0) = 0, \quad \xi \in Q, \quad j = 1,2,3, \end{cases}$$

where $\eta^j(t) = 2\int_\Omega \mathrm{Im}[(\Psi^0)^*(\frac{\partial}{\partial x_j} - \mathrm{i}\mathbf{A}^0_j)\Psi^0]d\mathbf{x}/\int_\Omega \mathbf{A}^0_j|\Psi^0|^2 d\mathbf{x}$ with $\mathbf{A}^0_j$ being the jth component of $\mathbf{A}^0$.

Remark 2.6. The new cell function is defined when ε is not very small. Furthermore, the way to define the integral in $\eta^j(t)$ is not unique. For example, we can define the integral over a subdomain of Ω instead of the whole domain and avoid the denominator in $\eta^i(t)$ vanishing. Thus $\mathrm{M}^j(\xi,t)$ is well defined in (2.19).

The term on the right-hand side of (2.16), i.e.,

(2.20) $$2N\big(H(\xi) + H(\xi)\nabla_\xi\boldsymbol{\theta}(\xi) - \hat{H}\big)\mathrm{Im}\big[(\Psi^0)^*(\nabla_\mathbf{x} - \mathrm{i}\mathbf{A}^0)\Psi^0\big],$$

represents the difference between the leading term (zero order) in the expansion of the quantum current density $\mathbf{J}^\varepsilon$ and its integral average value over the reference cell (the homogenized quantum current density $\mathbf{J}^0$), which is the source of difficulty. Although it emerges as a zero-order term in the Maxwell equations (after substituting (2.1) into (2.14)), this term is ignored in the definition of the second-order cell function $\Theta_2(\xi)$; otherwise it will be difficult to find $\Theta_2(\xi)$. To pick it up, we introduce a new cell function $\mathrm{M}(\xi,t)$ in the multiscale expansion of $\mathbf{A}^\varepsilon$, reinsert the expansion in the Maxwell equations, and then identify powers of ε. Unlike the traditional cell functions, the new cell function $\mathrm{M}(\xi,t)$ is time-dependent and satisfies a Maxwell-type equation. If the coefficients matrix $H(\xi) = \big(h_{ij}(\xi)\big)$ is a constant matrix, i.e., $h_{ij}(\xi) \equiv const$, the term (2.20) vanishes and $\mathrm{M}(\xi,t) \equiv \mathbf{0}$. Therefore, the modified multiscale solution $\widetilde{\mathbf{A}}^\varepsilon$ is compatible with the original multiscale solutions since, in this case, the oscillation characteristic of the quantum current density $\mathbf{J}^\varepsilon$ can be neglected.

Now we define the modified first-order and second-order multiscale approximate solutions of $\mathbf{A}^\varepsilon$:

(2.21)
$$\tilde{\mathbf{A}}^\varepsilon_1(\mathbf{x},t) = (\mathrm{I} + \mathrm{M}(\xi,t,\varepsilon)\rho^0)\mathbf{A}^0(\mathbf{x},t) + \varepsilon\Theta_1(\xi)\nabla \times \mathbf{A}^0(\mathbf{x},t),$$
$$\tilde{\mathbf{A}}^\varepsilon_2(\mathbf{x},t) = \tilde{\mathbf{A}}^\varepsilon_1(\mathbf{x},t) + \varepsilon^2\Theta_2(\xi)\nabla \times (\nabla \times \mathbf{A}^0(\mathbf{x},t)).$$

3. Finite element computations. In this section, we discuss the finite element computations of the homogenized Maxwell–Schrödinger system (2.10) and the cell functions $\theta_m(\xi), \theta_{ml}(\xi), \Theta_1(\xi), \Theta_2(\xi)$, and $\mathrm{M}(\xi,t)$.

3.1. Finite element computations of the cell functions. For the scalar cell equations (2.3) and (2.5), we employ the adaptive Lagrangian finite element method to solve them. The computational details can be found in [34]. For the vector cell equations (2.4) and (2.7), we apply the Nédélec edge finite element combined with an adaptive multilevel method to solve them. For more computational details and error analysis, we refer the reader to [6, 34].

Since the new cell equation (2.19) is formally similar to the time-dependent Maxwell equations in second-order formulation, it can be solved by the numerical

algorithms developed for the Maxwell equations. In this paper, we discretize it by using the edge element in space together with the symplectic geometric scheme in time as described in [35].

3.2. Numerical algorithms for the homogenized Maxwell–Schrödinger system. In this section, we present the fully discrete finite element method for the homogenized Maxwell–Schrödinger system (2.10) and establish the stability estimates. The existence and uniqueness of solutions to the discrete system are proved. For the sake of brevity, we omit the superscripts 0 of the functions for the homogenized Maxwell–Schrödinger system in this section. Furthermore, we assume that Ω is a bounded Lipschitz polyhedron domain.

To begin, we introduce some notation. Let $H^s(\Omega)$ ($s \in \mathbb{N}^+$) and $L^p(\Omega)$ ($p \geq 1$) be the standard Sobolev spaces and Lebesgue spaces of the real-valued functions defined in Ω, and let $H_0^s(\Omega)$ be the subspace of $H^s(\Omega)$ consisting of functions whose traces vanish on the boundary $\partial\Omega$. Sobolev spaces and Lebesgue spaces of the complex-valued functions are denoted by $\mathcal{H}^s(\Omega) = \{u + \mathrm{i}v \,|\, u, v \in H^s(\Omega)\}$ and $\mathcal{L}^p(\Omega) = \{u + \mathrm{i}v \,|\, u, v \in L^p(\Omega)\}$, respectively. Moreover, we denote $\mathbf{L}^p(\Omega) = [L^p(\Omega)]^3$ as Lebesgue spaces of the vector-valued functions. The dual spaces of $\mathcal{H}_0^s(\Omega)$ and $H_0^s(\Omega)$ are denoted by $\mathcal{H}^{-s}(\Omega)$ and $H^{-s}(\Omega)$, respectively. L^2 inner-products in $L^2(\Omega)$, $\mathcal{L}^2(\Omega)$, and $\mathbf{L}^2(\Omega)$ are abbreviated by $(\cdot, \cdot)$ without ambiguity.

Furthermore, we define

$$(3.1) \quad \begin{aligned} &\mathbf{H}(\mathbf{curl}; \Omega) = \{\mathbf{u} \in \mathbf{L}^2(\Omega); \nabla \times \mathbf{u} \in \mathbf{L}^2(\Omega)\}, \\ &\mathbf{H}_0(\mathbf{curl}; \Omega) = \{\mathbf{u} \in \mathbf{H}(\mathbf{curl}; \Omega) \,;\, \mathbf{u} \times \mathbf{n} = 0 \ \text{on} \ \partial\Omega\}, \end{aligned}$$

which are equipped with the norm

$$\|\mathbf{u}\|_{\mathbf{H}(\mathbf{curl};\Omega)} = \|\mathbf{u}\|_{\mathbf{L}^2(\Omega)} + \|\nabla \times \mathbf{u}\|_{\mathbf{L}^2(\Omega)}.$$

The weak formulation of the homogenized Maxwell–Schrödinger system (2.10) can be formulated as follows: given $\Psi_0 \in \mathcal{H}_0^1(\Omega)$, $\mathbf{A}_0 \in \mathbf{H}_0(\mathbf{curl}; \Omega)$, and $\mathbf{A}_1 \in \mathbf{L}^2(\Omega)$, find $(\Psi, \mathbf{A}) \in \mathcal{H}_0^1(\Omega) \times \mathbf{H}_0(\mathbf{curl}; \Omega)$, such that for all $t \in (0, T)$, the equations

$$(3.2)$$
$$\begin{cases} \left(\mathrm{i}\dfrac{\partial\Psi}{\partial t}, \varphi\right) = \left(\hat{H}(\nabla - \mathrm{i}\mathbf{A})\Psi, (\nabla - \mathrm{i}\mathbf{A})\varphi\right) + \left(\langle V_c\rangle\Psi, \varphi\right) + \left(V_{xc}(N|\Psi|^2)\Psi, \varphi\right), \\ \left(\dfrac{\partial^2\mathbf{A}}{\partial t^2}, \mathbf{v}\right) + \left(\hat{B}\nabla \times \mathbf{A}, \nabla \times \mathbf{v}\right) - \left(2N\hat{H}\,\mathrm{Im}[(\Psi)^*(\nabla - \mathrm{i}\mathbf{A})\Psi], \mathbf{v}\right) = (\mathbf{J}_s, \mathbf{v}) \end{cases}$$

hold for any $(\varphi, \mathbf{v}) \in \mathcal{H}_0^1(\Omega) \times \mathbf{H}_0(\mathbf{curl}; \Omega)$.

Let $\mathcal{T}_h = \{K\}$ be a quasi-uniform partition of Ω into tetrahedrons of maximal diameter h. For a given partition $\mathcal{T}_h$, we define the linear finite element subspaces of $H_0^1(\Omega)$ and $\mathcal{H}_0^1(\Omega)$,

$$(3.3) \qquad V_h = \{u_h \in H_0^1(\Omega): \ u_h|_K \in P_1 \ \forall K \in \mathcal{T}_h\}, \quad \mathcal{V}_h = V_h \oplus \mathrm{i}V_h,$$

and the Nédélec finite element subspace of $\mathbf{H}_0(\mathbf{curl}; \Omega)$ [23],

$$(3.4) \qquad \mathbf{V}_h = \{\mathbf{u}_h \in \mathbf{H}_0(\mathbf{curl}; \Omega): \ \mathbf{u}_h|_K \in R_1 \ \forall K \in \mathcal{T}_h\},$$

where

$$P_1 = \{a + \mathbf{b} \cdot \mathbf{x}: \ a \in \mathbb{R}, \ \mathbf{b} \in \mathbb{R}^3\}, \quad R_1 = \{\mathbf{a} + \mathbf{b} \times \mathbf{x}: \ \mathbf{a}, \mathbf{b} \in \mathbb{R}^3\}.$$

For $\psi \in \mathcal{H}_0^1(\Omega)$, let $\mathcal{R}_h\psi$ be the Ritz projection of ψ onto $\mathcal{V}_h$ which satisfies

$$(3.5) \qquad \big(\nabla(\mathcal{R}_h\psi - \psi),\, \nabla\varphi\big) = 0 \quad \forall\, \varphi \in \mathcal{V}_h.$$

Similarly, for $\mathbf{u} \in \mathbf{L}^2(\Omega)$, we let $\mathbf{P}_h\mathbf{u}$ denote the $\mathbf{L}^2$ projection of $\mathbf{u}$ onto $\mathbf{V}_h$ satisfying

$$(3.6) \qquad \big(\mathbf{P}_h\mathbf{u} - \mathbf{u},\, \mathbf{v}\big) = 0 \quad \forall\, \mathbf{v} \in \mathbf{V}_h.$$

To define our fully discrete scheme, we partition the time interval $(0, T)$ into M uniform subintervals using the nodal points

$$0 = t^0 < t^1 < \cdots < t^M = T,$$

with $t^k = k\tau$ and $\tau = T/M$. We denote $u^k = u(\cdot, t^k)$ for any given functions $u \in C\big((0,T); W\big)$ with a Banach space W. For a given sequence $\{u^k\}_{k=0}^M$, we introduce the following notation:

$$(3.7) \qquad \begin{aligned} \partial_\tau u^k &= (u^k - u^{k-1})/\tau, \quad \partial_\tau^2 u^k = (\partial_\tau u^k - \partial_\tau u^{k-1})/\tau, \\ \overline{u}^k &= (u^k + u^{k-1})/2, \qquad \widetilde{u}^k = (\overline{u}^k + \overline{u}^{k-1})/2. \end{aligned}$$

Here the superscript k denotes the exact value instead of the approximation at time t^k.

For convenience, we assume that the vector potential $\mathbf{A}$ is defined in the interval $[-\tau, T]$ in terms of the time variable t. Using the above notation, we now give the fully discrete scheme for the homogenized Maxwell–Schrödinger system:

$$(3.8) \qquad \Psi_h^0 = \mathcal{R}_h\Psi_0, \quad \mathbf{A}_h^0 = \mathbf{P}_h\mathbf{A}_0, \quad \mathbf{A}_h^0 - \mathbf{A}_h^{-1} = \tau\mathbf{P}_h\mathbf{A}_1,$$

and we find $(\Psi_h^k, \mathbf{A}_h^k) \in \mathcal{V}_h \times \mathbf{V}_h$ such that for $k = 1, 2, \ldots, M$,

$$(3.9)$$
$$\begin{cases} -\mathrm{i}\big(\partial_\tau\Psi_h^k,\, \varphi\big) + \big(\hat{H}(\nabla - \mathrm{i}\overline{\mathbf{A}}_h^k)\overline{\Psi}_h^k,\, (\nabla - \mathrm{i}\overline{\mathbf{A}}_h^k)\varphi\big) + \big(\langle V_c\rangle\overline{\Psi}_h^k,\, \varphi\big) + \big(\mathcal{G}(\Psi_h^k,\, \Psi_h^{k-1})\,\overline{\Psi}_h^k,\, \varphi\big) \\ \hspace{9cm} = 0 \quad \forall\varphi \in \mathcal{V}_h, \\[1ex] \big(\partial_\tau^2\mathbf{A}_h^k,\, \mathbf{v}\big) + \big(\hat{B}\,\nabla \times (\mathbf{A}_h^k + \mathbf{A}_h^{k-2})/2,\, \nabla \times \mathbf{v}\big) - \big(2N\hat{H}\,\mathrm{Im}[(\Psi_h^{k-1})^*(\nabla - \mathrm{i}\widetilde{\mathbf{A}}_h^k)\Psi_h^{k-1}],\, \mathbf{v}\big) \\ \hspace{9cm} = \big(\mathbf{J}_s^{k-1},\, \mathbf{v}\big) \quad \forall\mathbf{v} \in \mathbf{V}_h, \end{cases}$$

where

$$(3.10) \qquad \mathcal{G}(\Psi_h^k,\, \Psi_h^{k-1}) = \frac{G(N|\Psi_h^k|^2) - G(N|\Psi_h^{k-1}|^2)}{N(|\Psi_h^k|^2 - |\Psi_h^{k-1}|^2)}$$

and G is an antiderivative of V_{xc}, i.e., $G'(s) = V_{xc}(s) \ \forall s \in \mathbb{R}$.

Remark 3.1. The technique for the numerical discretization of $V_{xc}(N|\Psi|^2)$ in the Schrödinger equation was first used by Strauss and Vázquez [27] for the nonlinear Klein–Gordon equation and was later applied to the cubic nonlinear Schrödinger equation by Delfour, Fortin, and Payne [13]. This scheme is favored mainly because it can preserve the energy of the discrete system. Note that

$$(3.11) \qquad \mathcal{G}(\Psi_h^k,\, \Psi_h^{k-1}) = \int_0^1 V_{xc}\big(\lambda N|\Psi_h^k|^2 + (1-\lambda)N|\Psi_h^{k-1}|^2\big)\, \mathrm{d}\lambda.$$

We can replace the quotient with the right-hand side term of (3.11) in the case of vanishing denominator.

Remark 3.2. In practical computation, we should replace the homogenized matrices $\hat{H}$ and $\hat{B}$ defined in (2.6) and (2.8) with
(3.12)
$$\hat{H}^{h_0} = \int_Q \big(H(\xi) + H(\xi)\nabla_\xi \boldsymbol{\theta}^{h_0}(\xi)\big)d\xi, \quad \hat{B}^{h_0} = \int_Q \big(B(\xi) + B(\xi)\nabla_\xi \times \Theta_1^{h_0}(\xi)\big)d\xi,$$

where $\boldsymbol{\theta}^{h_0}(\xi)$ and $\Theta_1^{h_0}(\xi)$ are the numerical solutions of the cell functions $\boldsymbol{\theta}(\xi)$ and $\Theta_1(\xi)$, respectively. It has been proved in [6, 34] that if h_0 is sufficiently small, then

(3.13)
$$\|\hat{H}^{h_0} - \hat{H}\|_F \le Ch_0^2, \quad \|\hat{B}^{h_0} - \hat{B}\|_F \le Ch_0^2,$$

where $\|B\|_F$ denotes the Frobenius norm of the matrix B. The error between $(\Psi_h^k, \mathbf{A}_h^k)$ and $(\Psi_{h,h_0}^k, \mathbf{A}_{h,h_0}^k)$, where $(\Psi_{h,h_0}^k, \mathbf{A}_{h,h_0}^k)$ is the solution of (3.9) with $\hat{H}$ and $\hat{B}$ replaced by $\hat{H}^{h_0}$ and $\hat{B}^{h_0}$, respectively, will be investigated in our future work. For convenience, we drop the superscript h_0 and still use $\hat{H}$ and $\hat{B}$ in this section.

At each time level, we first solve the discrete Maxwell equations $(3.9)_2$ to get $\mathbf{A}_h^k$, insert it into the discrete Schrödinger equation $(3.9)_1$, and then solve the equation to obtain Ψ_h^k. Thus the solution of the discrete system (3.9) can be obtained by solving the two equations alternately. Due to the exchange-correlation function V_{xc}, the discrete Schrödinger equation is a nonlinear equation whose solvability will be proved later. Next we derive some stability estimates for the solution of the discrete system (3.9). We first define the energy of the discrete system as follows:

(3.14)
$$E_h^k = N\big(\hat{H}(\nabla - i\overline{\mathbf{A}}_h^k)\Psi_h^k, \, (\nabla - i\overline{\mathbf{A}}_h^k)\Psi_h^k\big) + N\langle V_c\rangle\|\Psi_h^k\|_{\mathcal{L}^2}^2 + \int_\Omega G(N|\Psi_h^k|^2)\, d\mathbf{x}$$
$$+ \frac{1}{2}\|\partial_\tau \mathbf{A}_h^k\|_{\mathbf{L}^2}^2 + \frac{1}{4}\big(\hat{B}\nabla \times \mathbf{A}_h^k, \, \nabla \times \mathbf{A}_h^k\big) + \frac{1}{4}\big(\hat{B}\nabla \times \mathbf{A}_h^{k-1}, \, \nabla \times \mathbf{A}_h^{k-1}\big).$$

To prove the stability estimates, we need Kato's inequality.

LEMMA 3.1 (Kato's inequality [20]). *Supposing that* $\mathbf{A} \in \mathbf{L}_{\mathrm{loc}}^2(\mathbb{R}^3)$, $f \in \mathcal{L}^2(\mathbb{R}^3)$, *and* $(\nabla - i\mathbf{A})f \in \mathbf{L}^2(\mathbb{R}^3)$, *then* $|f|$, *the modulus of* f, *is in* $H^1(\mathbb{R}^3)$ *and the diamagnetic inequality holds pointwise for almost every* $\mathbf{x} \in \mathbb{R}^3$:

$$\big|\nabla|f|(\mathbf{x})\big| \le |(\nabla - i\mathbf{A})f(\mathbf{x})|.$$

LEMMA 3.2. *For* $k = 1, 2, \ldots, M$, *we have*

(3.15)
$$\|\Psi_h^k\|_{\mathcal{L}^2} = \|\Psi_h^0\|_{\mathcal{L}^2}.$$

If G *satisfies* $\forall s \in \mathbb{R}^+$, $G(s) \ge 0$, *or* $|G(s)| \le C(1 + |s|^p)$, $0 \le p < \frac{5}{3}$, *then*

(3.16)
$$\|\nabla|\Psi_h^k|\|_{\mathbf{L}^2} + \|\Psi_h^k\|_{\mathcal{L}^6} + \|\mathbf{A}_h^k\|_{\mathbf{H}(\mathbf{curl};\Omega)} \le C,$$

where C *is a positive constant independent of* h *and* τ.

Proof. By choosing $\varphi = \overline{\Psi}_h^k$ in the first equation of (3.9) and taking the imaginary part, we obtain (3.15). Next we set $\varphi = \partial_\tau \Psi_h^k$ in the same equation and take the real part to get
(3.17)
$$2\,\mathrm{Re}\big[\big(\hat{H}(\nabla - i\overline{\mathbf{A}}_h^k)\overline{\Psi}_h^k, \, (\nabla - i\overline{\mathbf{A}}_h^k)\partial_\tau \Psi_h^k\big)\big] + \partial_\tau\big(\langle V_c\rangle\|\Psi_h^k\|_{\mathcal{L}^2}^2 + \frac{1}{N}\int_\Omega G(N|\Psi_h^k|^2)\, d\mathbf{x}\big) = 0,$$

where we have used the facts

$$\mathrm{Re}\big[(\langle V_c\rangle\overline{\Psi}_h^k,\,\partial_\tau\Psi_h^k)\big] = \frac{\langle V_c\rangle}{2\tau}\big(\|\Psi_h^k\|_{\mathcal{L}^2}^2 - \|\Psi_h^{k-1}\|_{\mathcal{L}^2}^2\big),$$
$$\mathrm{Re}\big[(\mathcal{G}(\Psi_h^k,\,\Psi_h^{k-1})\overline{\Psi}_h^k,\,\partial_\tau\Psi_h^k)\big] = \frac{1}{2N\tau}\int_\Omega \big(G(N|\Psi_h^k|^2) - G(N|\Psi_h^{k-1}|^2)\big)\,\mathrm{d}\mathbf{x}.$$

Now we turn to the analysis of the first term of (3.17). It is easy to see that
(3.18)
$$\mathrm{Re}\big[(\hat{H}(\nabla - \mathrm{i}\overline{\mathbf{A}}_h^k)\overline{\Psi}_h^k,\,(\nabla - \mathrm{i}\overline{\mathbf{A}}_h^k)\partial_\tau\Psi_h^k)\big] = \frac{1}{2}\partial_\tau\big(\hat{H}(\nabla - \mathrm{i}\overline{\mathbf{A}}_h^k)\Psi_h^k,\,(\nabla - \mathrm{i}\overline{\mathbf{A}}_h^k)\Psi_h^k)$$
$$+ \frac{1}{2\tau}\big[(\hat{H}(\nabla - \mathrm{i}\overline{\mathbf{A}}_h^{k-1})\Psi_h^{k-1},\,(\nabla - \mathrm{i}\overline{\mathbf{A}}_h^{k-1})\Psi_h^{k-1}) - (\hat{H}(\nabla - \mathrm{i}\overline{\mathbf{A}}_h^k)\Psi_h^{k-1},\,(\nabla - \mathrm{i}\overline{\mathbf{A}}_h^k)\Psi_h^{k-1})\big]$$
$$+ \frac{1}{2\tau}\mathrm{Re}\big[(\hat{H}(\nabla - \mathrm{i}\overline{\mathbf{A}}_h^k)\Psi_h^{k-1},\,(\nabla - \mathrm{i}\overline{\mathbf{A}}_h^k)\Psi_h^k) - (\hat{H}(\nabla - \mathrm{i}\overline{\mathbf{A}}_h^k)\Psi_h^k,\,(\nabla - \mathrm{i}\overline{\mathbf{A}}_h^k)\Psi_h^{k-1})\big].$$

It is obvious that the last term on the right-hand side of (3.18) vanishes. By a tedious calculation, we find
(3.19)
$$\big(\hat{H}(\nabla - \mathrm{i}\overline{\mathbf{A}}_h^{k-1})\Psi_h^{k-1},\,(\nabla - \mathrm{i}\overline{\mathbf{A}}_h^{k-1})\Psi_h^{k-1}\big) - \big(\hat{H}(\nabla - \mathrm{i}\overline{\mathbf{A}}_h^k)\Psi_h^{k-1},\,(\nabla - \mathrm{i}\overline{\mathbf{A}}_h^k)\Psi_h^{k-1}\big)$$
$$= 2\big(\hat{H}\,\mathrm{Im}[(\Psi_h^{k-1})^*(\nabla - \mathrm{i}\widetilde{\mathbf{A}}_h^k)\Psi_h^{k-1}],\,\overline{\mathbf{A}}_h^k - \overline{\mathbf{A}}_h^{k-1}\big).$$

Substituting (3.18) and (3.19) into (3.17), we obtain

(3.20)
$$\partial_\tau\Big(\big(\hat{H}(\nabla - \mathrm{i}\overline{\mathbf{A}}_h^k)\Psi_h^k,\,(\nabla - \mathrm{i}\overline{\mathbf{A}}_h^k)\Psi_h^k\big) + \langle V_c\rangle\|\Psi_h^k\|_{\mathcal{L}^2}^2 + \frac{1}{N}\int_\Omega G(N|\Psi_h^k|^2)\,\mathrm{d}\mathbf{x}\Big)$$
$$+ \big(2\hat{H}\,\mathrm{Im}[(\Psi_h^{k-1})^*(\nabla - \mathrm{i}\widetilde{\mathbf{A}}_h^k)\Psi_h^{k-1}],\,\partial_\tau\overline{\mathbf{A}}_h^k\big) = 0.$$

To proceed further, we take $\mathbf{v} = \partial_\tau\overline{\mathbf{A}}_h^k = \overline{\partial_\tau\mathbf{A}_h^k}$ in the second equation of (3.9) to find

(3.21)
$$\partial_\tau\Big(\frac{1}{2}\|\partial_\tau\mathbf{A}_h^k\|_{\mathbf{L}^2}^2 + \frac{1}{4}\big(\hat{B}\nabla\times\mathbf{A}_h^k,\,\nabla\times\mathbf{A}_h^k\big) + \frac{1}{4}\big(\hat{B}\nabla\times\mathbf{A}_h^{k-1},\,\nabla\times\mathbf{A}_h^{k-1}\big)\Big)$$
$$- \big(2N\hat{H}\,\mathrm{Im}[(\Psi_h^{k-1})^*(\nabla - \mathrm{i}\widetilde{\mathbf{A}}_h^k)\Psi_h^{k-1}],\,\partial_\tau\overline{\mathbf{A}}_h^k\big) = \big(\mathbf{J}_s^{k-1},\,\partial_\tau\overline{\mathbf{A}}_h^k\big).$$

Multiplying (3.20) by N, adding it to (3.21), and recalling the definition of E_h^k in (3.14), we arrive at

(3.22)
$$\partial_\tau E_h^k = \big(\mathbf{J}_s^{k-1},\,\partial_\tau\overline{\mathbf{A}}_h^k\big),$$

which leads to

(3.23)
$$E_h^n = E_h^0 + \tau\sum_{k=1}^n\big(\mathbf{J}_s^{k-1},\,\partial_\tau\overline{\mathbf{A}}_h^k\big) \le C + \frac{\tau}{2}\sum_{k=1}^n\|\partial_\tau\mathbf{A}_h^k\|_{\mathbf{L}^2}^2 \quad \forall 1 \le n \le M.$$

Note that the homogenized matrices $\hat{H}$ and $\hat{B}$ are positive definite. Thus there exist constants C_1 and C_2 such that

(3.24)
$$\big(\hat{H}(\nabla - \mathrm{i}\overline{\mathbf{A}}_h^n)\Psi_h^n,\,(\nabla - \mathrm{i}\overline{\mathbf{A}}_h^n)\Psi_h^n\big) \ge C_1\|(\nabla - \mathrm{i}\overline{\mathbf{A}}_h^n)\Psi_h^n\|_{\mathbf{L}^2}^2,$$
$$\big(\hat{B}\nabla\times\mathbf{A}_h^n,\,\nabla\times\mathbf{A}_h^n\big) \ge C_2\|\nabla\times\mathbf{A}_h^n\|_{\mathbf{L}^2}^2.$$

Applying (3.24) to (3.23) and using (3.15), we have

$$
(3.25) \quad
\begin{aligned}
&C_1 \|(\nabla - \mathrm{i}\overline{\mathbf{A}}_h^n)\Psi_h^n\|_{\mathbf{L}^2}^2 + \frac{1}{2}\|\partial_\tau \mathbf{A}_h^n\|_{\mathbf{L}^2}^2 + \frac{C_2}{4}\|\nabla \times \mathbf{A}_h^n\|_{\mathbf{L}^2}^2 \\
&\qquad \leq C + \frac{\tau}{2}\sum_{k=1}^n \|\partial_\tau \mathbf{A}_h^k\|_{\mathbf{L}^2}^2 - \int_\Omega G(N|\Psi_h^n|^2)\,\mathrm{d}\mathbf{x}.
\end{aligned}
$$

If for all $s \in \mathbb{R}^+$, $|G(s)| \leq C(1 + |s|^p)$, then

$$
(3.26) \quad \left| \int_\Omega G(N|\Psi_h^n|^2)\,\mathrm{d}\mathbf{x} \right| \leq C + C\|\Psi_h^n\|_{\mathcal{L}^{2p}}^{2p}.
$$

It follows from the Gagliardo–Nirenberg inequality [17], Kato's inequality, and Young's inequality that

$$
(3.27) \quad
\begin{aligned}
C\|\Psi_h^n\|_{\mathcal{L}^{2p}}^{2p} &\leq C\|\nabla|\Psi_h^n|\|_{\mathbf{L}^2}^{3(p-1)}\|\Psi_h^n\|_{\mathcal{L}^2}^{3-p} \leq \frac{C_1}{2}\|\nabla|\Psi_h^n|\|_{\mathbf{L}^2}^2 + C\|\Psi_h^n\|_{\mathcal{L}^2}^{\frac{2(3-p)}{5-3p}} \\
&\leq \frac{C_1}{2}\|(\nabla - \mathrm{i}\overline{\mathbf{A}}_h^n)\Psi_h^n\|_{\mathbf{L}^2}^2 + C,
\end{aligned}
$$

where we have used the assumption that $0 \leq p < \frac{5}{3}$. Substituting (3.26) and (3.27) into (3.25), we obtain

$$
(3.28)
$$
$$
\frac{C_1}{2}\|(\nabla - \mathrm{i}\overline{\mathbf{A}}_h^n)\Psi_h^n\|_{\mathbf{L}^2}^2 + \frac{1}{2}\|\partial_\tau \mathbf{A}_h^n\|_{\mathbf{L}^2}^2 + \frac{C_2}{4}\|\nabla \times \mathbf{A}_h^n\|_{\mathbf{L}^2}^2 \leq C + \frac{\tau}{2}\sum_{k=1}^n \|\partial_\tau \mathbf{A}_h^k\|_{\mathbf{L}^2}^2.
$$

If for all $s \in \mathbb{R}^+$, $G(s) \geq 0$, we also have (3.28). Without loss of generality, we assume that $\tau < 1$. Now applying the discrete Gronwall inequality to (3.28), we have

$$
(3.29) \quad \|(\nabla - \mathrm{i}\overline{\mathbf{A}}_h^k)\Psi_h^k\|_{\mathbf{L}^2} + \|\mathbf{A}_h^k\|_{\mathbf{H}(\mathbf{curl};\Omega)} \leq C, \quad k = 1, 2, \ldots, M.
$$

Using (3.29) together with Sobolev's inequaltiy and Kato's inequality, we complete the proof of (3.16). □

Remark 3.3. Equation (3.22) implies that if $\mathbf{J}_s = 0$, then the energy of the discrete system is preserved.

Next we establish the existence and uniqueness of solutions to the discrete system (3.9).

LEMMA 3.3. *For $k = 1, 2, \ldots, M$, there exists a solution $\left(\Psi_h^k, \mathbf{A}_h^k\right)$ to the discrete system* (3.9). *Under the assumption of Lemma* 3.2, *if V_{xc} satisfies*

$$
(3.30) \quad \forall s_1, s_2 \in \mathbb{R}^+, |V_{xc}(s_1) - V_{xc}(s_2)| \leq C(1 + |s_1|^p + |s_2|^p)|s_1 - s_2|, \ p \geq 0,
$$

and $\tau h^{-2(p+1)}$ is sufficiently small, then the solution is unique.

Proof. Since the two equations of (3.9) can be solved alternately at each time level and it is not difficult to show that $(3.9)_2$ has a unique solution, we only need to consider the solvability of $(3.9)_1$. The existence of solutions can be proved by using the (Browder) fixed point theorem, and we refer the reader to [29] for more details. Next we consider the uniqueness of solutions to $(3.9)_1$.

Let Ψ_h^k and ψ_h^k be two solutions of $(3.9)_1$. Set $\eta_h^k = \Psi_h^k - \psi_h^k$. It satisfies

$$
\begin{aligned}
\mathrm{i}\big(\eta_h^k,\, \varphi\big) &= \frac{\tau}{2}\big(\hat{H}(\nabla - \mathrm{i}\overline{\mathbf{A}}_h^k)\eta_h^k,\, (\nabla - \mathrm{i}\overline{\mathbf{A}}_h^k)\varphi\big) + \frac{\tau}{2}\big(\langle V_c\rangle\eta_h^k,\, \varphi\big) \\
&\quad + \frac{\tau}{4}\big(\big(\mathcal{G}(\Psi_h^k,\, \Psi_h^{k-1}) - \mathcal{G}(\psi_h^k,\, \Psi_h^{k-1})\big)\,(\Psi_h^k + \psi_h^k + 2\Psi_h^{k-1}),\, \varphi\big) \\
&\quad + \frac{\tau}{4}\big(\big(\mathcal{G}(\Psi_h^k,\, \Psi_h^{k-1}) + \mathcal{G}(\psi_h^k,\, \Psi_h^{k-1})\big)\,\eta_h^k,\, \varphi\big) \quad \forall \varphi \in \mathcal{V}_h.
\end{aligned}
\tag{3.31}
$$

Choosing $\varphi = \eta_h^k$ in (3.31) and taking the imaginary part, we have

$$
\|\eta_h^k\|_{\mathcal{L}^2}^2 \le \frac{\tau}{4}\big|\big(\big(\mathcal{G}(\Psi_h^k,\, \Psi_h^{k-1}) - \mathcal{G}(\psi_h^k,\, \Psi_h^{k-1})\big)\,(\Psi_h^k + \psi_h^k + 2\Psi_h^{k-1}),\, \eta_h^k\big)\big|.
\tag{3.32}
$$

By using (3.11) and (3.30), we find

$$
\big|\big(\mathcal{G}(\Psi_h^k,\, \Psi_h^{k-1}) - \mathcal{G}(\psi_h^k,\, \Psi_h^{k-1})\big)\big| \le C\big(1 + |\Psi_h^k|^{2p} + |\psi_h^k|^{2p} + |\Psi_h^{k-1}|^{2p}\big)\,(|\Psi_h^k| + |\psi_h^k|)\,|\eta_h^k|.
\tag{3.33}
$$

Applying (3.33) to (3.32), we arrive at

$$
\begin{aligned}
\|\eta_h^k\|_{\mathcal{L}^2}^2 &\le C\tau\big(\|\Psi_h^k\|_{\mathcal{L}^\infty}^{2p+2} + \|\psi_h^k\|_{\mathcal{L}^\infty}^{2p+2} + \|\Psi_h^{k-1}\|_{\mathcal{L}^\infty}^{2p+2}\big)\|\eta_h^k\|_{\mathcal{L}^2}^2 \\
&\quad + C\tau\big(\|\Psi_h^k\|_{\mathcal{L}^\infty}^2 + \|\psi_h^k\|_{\mathcal{L}^\infty}^2 + \|\Psi_h^{k-1}\|_{\mathcal{L}^\infty}^2\big)\|\eta_h^k\|_{\mathcal{L}^2}^2,
\end{aligned}
\tag{3.34}
$$

which leads to

$$
\begin{aligned}
\|\eta_h^k\|_{\mathcal{L}^2}^2 &\le C\tau h^{-2(p+1)}\big(\|\Psi_h^k\|_{L^6}^{2p+2} + \|\psi_h^k\|_{L^6}^{2p+2} + \|\Psi_h^{k-1}\|_{L^6}^{2p+2}\big)\|\eta_h^k\|_{\mathcal{L}^2}^2 \\
&\le C\tau h^{-2(p+1)}\big(\|\nabla|\Psi_h^k|\|_{\mathbf{L}^2}^{2p+2} + \|\nabla|\psi_h^k|\|_{\mathbf{L}^2}^{2p+2} + \|\nabla|\Psi_h^{k-1}|\|_{\mathbf{L}^2}^{2p+2}\big)\|\eta_h^k\|_{\mathcal{L}^2}^2 \\
&\le C\tau h^{-2(p+1)}\|\eta_h^k\|_{\mathcal{L}^2}^2
\end{aligned}
\tag{3.35}
$$

by an application of Lemma 3.2 and the following inverse inequality [5]:

$$
\|u_h\|_{L^\infty} \le Ch^{-1}\|u_h\|_{L^6} \quad \forall\, u_h \in V_h.
\tag{3.36}
$$

Therefore, if $C\tau h^{-2(p+1)} < 1$, we have $\eta_h^k = 0$ and obtain the uniqueness of solutions to $(3.9)_1$. □

In practical computation, $(3.9)_1$ can be solved by Picard or Newton iteration. Let tol be the tolerance for the nonlinear iteration. At the time level k, if $\overline{\mathbf{A}}_h^k$ and Ψ_h^{k-1} are available, then we have the following Picard iteration algorithm:

Algorithm (Picard Iteration).
    1: Given $\overline{\mathbf{A}}_h^k$, Ψ_h^{k-1}, set $\Psi_h^{k,0} = \overline{\Psi}_h^{k-1}$.

    2: For $l = 0, 1, 2, \ldots$, do

      (1): Solve the equation

$$
\begin{aligned}
&-\mathrm{i}\left(\frac{\Psi_h^{k,l+1} - \Psi_h^{k-1}}{\tau},\, \varphi\right) + \left(\hat{H}(\nabla - \mathrm{i}\overline{\mathbf{A}}_h^k)\frac{\Psi_h^{k,l+1} + \Psi_h^{k-1}}{2},\, (\nabla - \mathrm{i}\overline{\mathbf{A}}_h^k)\varphi\right) \\
&+ \left(\langle V_c\rangle\frac{\Psi_h^{k,l+1} + \Psi_h^{k-1}}{2},\, \varphi\right) + \left(\mathcal{G}(\Psi_h^{k,l},\, \Psi_h^{k-1})\frac{\Psi_h^{k,l+1} + \Psi_h^{k-1}}{2},\, \varphi\right) = 0 \;\; \forall\varphi \in \mathcal{V}_h.
\end{aligned}
\tag{3.37}
$$

      (2): If $\|\Psi_h^{k,l+1} - \Psi_h^{k,l}\|_{\mathcal{H}^1} \le$ tol, then break.

    3: Update solution: $\Psi_h^k = \Psi_h^{k,l+1}$.
Now we show the convergence of the nonlinear iteration.

LEMMA 3.4. *Assume that V_{xc} satisfies* (3.30). *If $\tau h^{-3(p+1)}$ is sufficiently small, then the sequence $\{\Psi_h^{k,l}\}_{l=1}^{\infty}$ generated by the Picard iteration converges to the unique solution of* (3.9)$)_1$.

Proof. It is easy to see that $\forall l \geq 1$, $\|\Psi_h^{k,l}\|_{\mathcal{L}^2} = \|\Psi_h^{k-1}\|_{\mathcal{L}^2}$. Define $\mathcal{E}_h^{l+1} = \Psi_h^{k,l+1} - \Psi_h^{k,l}$. By subtracting the equation (3.37) for $\Psi_h^{k,l+1}$ from the equation for $\Psi_h^{k,l}$ and using an argument similar to that in Lemma 3.3, we have
(3.38)
$$\begin{aligned}
\|\mathcal{E}_h^{l+1}\|_{\mathcal{L}^2} &\leq C\tau\big(\|\Psi_h^{k,l+1}\|_{\mathcal{L}^\infty}^{2p+2} + \|\Psi_h^{k,l}\|_{\mathcal{L}^\infty}^{2p+2} + \|\Psi_h^{k,l-1}\|_{\mathcal{L}^\infty}^{2p+2} + \|\Psi_h^{k-1}\|_{\mathcal{L}^\infty}^{2p+2}\big)\|\mathcal{E}_h^l\|_{\mathcal{L}^2} \\
&\quad + C\tau\big(\|\Psi_h^{k,l+1}\|_{\mathcal{L}^\infty}^2 + \|\Psi_h^{k,l-1}\|_{\mathcal{L}^\infty}^2 + \|\Psi_h^{k,l-1}\|_{\mathcal{L}^\infty}^2 + \|\Psi_h^{k-1}\|_{\mathcal{L}^\infty}^2\big)\|\mathcal{E}_h^l\|_{\mathcal{L}^2} \\
&\leq C\tau h^{-3(p+1)}\|\mathcal{E}_h^l\|_{\mathcal{L}^2},
\end{aligned}$$

where we have used the inverse inequality [5]

(3.39)
$$\|u_h\|_{L^\infty} \leq Ch^{-\frac{3}{2}}\|u_h\|_{L^2} \quad \forall\, u_h \in V_h.$$

If $C\tau h^{-3(p+1)} \leq \frac{1}{2}$, then (3.38) implies that the sequence $\{\Psi_h^{k,l}\}_{l=1}^{\infty}$ is a Cauchy sequence and thus converges. □

4. Multiscale numerical algorithm and numerical examples. In this section, we first summarize the multiscale numerical algorithm for the Maxwell–Schrödinger system (1.11) and then provide some numerical examples to validate our method.

As described in section 2, the multiscale numerical algorithm consists of the following steps:

Step I: Compute the cell functions $\theta_m(\xi), \theta_{ml}(\xi), \Theta_1(\xi), \Theta_2(\xi)$ in the unit cell $Q = (0,1)^3$ by solving the cell equations, and then compute the homogenized coefficients matrices $\hat{H}$ and $\hat{B}$ via (2.6) and (2.8), respectively.

Step II: For $k = 1, 2, \ldots, M$, do

(1) Solve the homogenized Maxwell–Schrödinger system (2.10) in Ω at the time level k by the proposed scheme (3.9). Since the coefficients of the homogenized Maxwell–Schrödinger system are constants, we can solve it on a coarse spatial mesh.

(2) Apply higher-order difference quotients to compute the partial derivatives $\frac{\partial \Psi_h^k}{\partial x_m}$, $\frac{\partial^2 \Psi_h^k}{\partial x_m \partial x_l}$, $\nabla \times \mathbf{A}_h^k$, and $\nabla \times (\nabla \times \mathbf{A}_h^k)$ numerically, and form the multiscale approximate solutions (2.12)–(2.13), where $(\Psi_h^k, \mathbf{A}_h^k)$ is the numerical solution of the homogenized Maxwell–Schrödinger system at the time level k.

(3) If the oscillations of the quantum current density cannot be neglected in the Maxwell equations, compute the cell function M_h^k and form the modified multiscale solutions (2.21), where M_h^k is the numerical solution of (2.19) at the time level k.

Remark 4.1. In general, whether the oscillations of the quantum current density can be neglected or not depends on the relativistic size of the heterogeneities (ε), the number of the electrons (N), and the ratio of the effective mass of the semiconductor matrix to the heterogeneities (denoted by λ). If ε is sufficiently small, the oscillations of the quantum current density are smeared out. The larger N and the smaller λ, the more significant the oscillations of the quantum current density are. In our experience, in cases when $\varepsilon \geq 0.1$, $N \geq 5$, and $\lambda \leq 0.1$, the oscillations of the quantum current density cannot be neglected in the Maxwell equations.
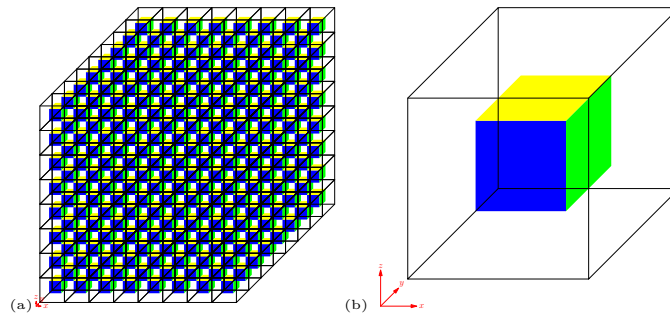
FIG. 4.1. (a) *The whole domain* $\Omega = (0,1)^3$. (b) *The unit cell Q.*

To validate the numerical algorithms presented above, we give some numerical examples.

Example 4.1. In this example, we consider the Maxwell–Schrödinger system (1.11) without the exchange-correlation potential, i.e., $V_{xc} = 0$. The whole domain Ω and the unit cell Q with $\varepsilon = 1/8$ are shown in Figure 4.1. Assume that the inclusion in the unit cell is a quantum dot. We take $N = 1$, $T = 0.5$, and the time step $\tau = 0.0025$. V_c and $\mathbf{J}_s$ are given as follows:

$$V_c\left(\frac{\mathbf{x}}{\varepsilon}\right) = \left\{ \begin{array}{l} 0 \text{ in each dot,} \\ 1 \text{ else,} \end{array} \right.$$

$$\mathbf{J}_s(\mathbf{x}, t) = \big(1000\sin(\pi t) + \sin(2\pi x_1)\sin(2\pi x_2)\cos(2\pi x_3)\big)(1, 1, 1)^{\mathrm{T}}.$$

We consider the following cases:

Case 4.1.1. $\quad h_{ij}\left(\dfrac{\mathbf{x}}{\varepsilon}\right) = \left\{ \begin{array}{l} 0.025\delta_{ij} \text{ in each dot,} \\ \delta_{ij} \text{ else,} \end{array} \right. \qquad b_{ij}\left(\dfrac{\mathbf{x}}{\varepsilon}\right) = \left\{ \begin{array}{l} \delta_{ij} \text{ in each dot,} \\ 100\delta_{ij} \text{ else,} \end{array} \right.$

Case 4.1.2. $\quad h_{ij}\left(\dfrac{\mathbf{x}}{\varepsilon}\right) = \left\{ \begin{array}{l} 0.025\delta_{ij} \text{ in each dot,} \\ \delta_{ij} \text{ else,} \end{array} \right. \qquad b_{ij}\left(\dfrac{\mathbf{x}}{\varepsilon}\right) = \left\{ \begin{array}{l} \delta_{ij} \text{ in each dot,} \\ 400\delta_{ij} \text{ else.} \end{array} \right.$

Here δ_{ij} is the Kronecker symbol.

TABLE 4.1
Comparison of computational costs to solve the Schrödinger equation.

	Original problem	Cell problem	Homogenized problem
Dof	2478213	180135	76410
Elements	13573655	1034688	403590
CPU time (s)	1518	11	53

TABLE 4.2
Comparison of computational costs to solve the Maxwell equations.

	Original problem	Cell problem	Homogenized problem
Dof	16125013	1229702	486888
Elements	13573655	1034688	403590
CPU time (s)	2756	24	74

TABLE 4.3

Comparison of computational results for Example 4.1: Relative errors in the approximation of the density function n^ε.

	$\frac{\|e_0\|_0}{\|n^\varepsilon\|_0}$	$\frac{\|e_1\|_0}{\|n^\varepsilon\|_0}$	$\frac{\|e_2\|_0}{\|n^\varepsilon\|_0}$	$\frac{\|e_0\|_1}{\|n^\varepsilon\|_1}$	$\frac{\|e_1\|_1}{\|n^\varepsilon\|_1}$	$\frac{\|e_2\|_1}{\|n^\varepsilon\|_1}$
Case 4.1.1	0.057851	0.054876	0.009288	0.478132	0.449785	0.064030
Case 4.1.2	0.060731	0.057940	0.011570	0.487747	0.460989	0.069483

TABLE 4.4

Comparison of computational results for Example 4.1: Relative errors in the approximation of the vector potential $\mathbf{A}^\varepsilon$.

	$\frac{\|\mathbf{e}_0\|_0}{\|\mathbf{A}^\varepsilon\|_0}$	$\frac{\|\mathbf{e}_1\|_0}{\|\mathbf{A}^\varepsilon\|_0}$	$\frac{\|\mathbf{e}_2\|_0}{\|\mathbf{A}^\varepsilon\|_0}$	$\frac{\|\mathbf{e}_0\|_1}{\|\mathbf{A}^\varepsilon\|_1}$	$\frac{\|\mathbf{e}_1\|_1}{\|\mathbf{A}^\varepsilon\|_1}$	$\frac{\|\mathbf{e}_2\|_1}{\|\mathbf{A}^\varepsilon\|_1}$
Case 4.1.1	0.083335	0.071058	0.029445	1.550864	1.062309	0.704374
Case 4.1.2	0.297918	0.293482	0.100150	5.307896	3.268900	0.896229
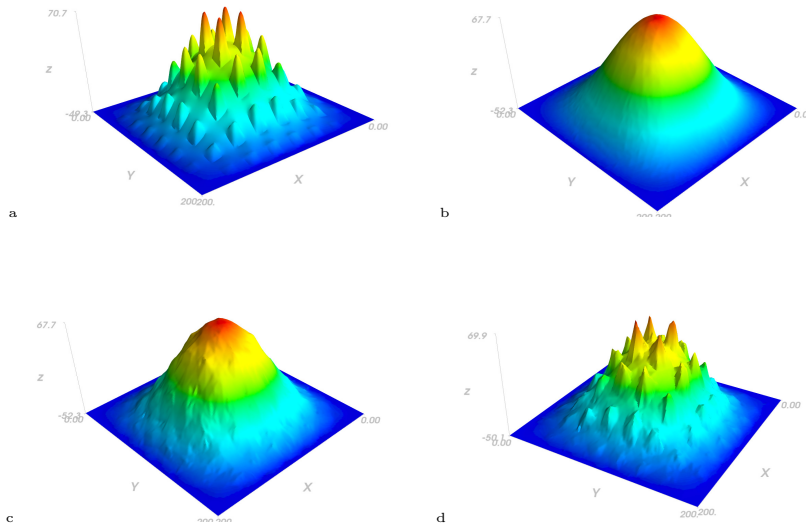
FIG. 4.2. *The density function on the intersection $x_3 = 0.4$ at time $t = 0.3$ in Case 4.1.1: (a) Reference solution n^ε in fine mesh; (b) homogenization solution n^0 in coarse mesh; (c) first-order multiscale solution $n^{\varepsilon,1}$; (d) second-order multiscale solution $n^{\varepsilon,2}$.*

We let Ψ_0 be the ground state wave function of the time-independent Schrödinger equation. For the computational details of Ψ_0, we refer the reader to [34]. We take $\mathbf{A}_0 = \mathbf{A}_1 = 0$.

In order to demonstrate the numerical accuracy of the multiscale method, we need the exact solution $\left(\mathbf{A}^\varepsilon(\mathbf{x}, t),\ \Psi^\varepsilon(\mathbf{x}, t)\right)$ of the Maxwell–Schrödinger system (1.11). Due to the discontinuous coefficients matrices $H(\frac{\mathbf{x}}{\varepsilon})$ and $B(\frac{\mathbf{x}}{\varepsilon})$ and the nonlinear nature of the system, it is extremely difficult, even impossible, to obtain the exact solution. Here, we replace the exact solution $\left(\mathbf{A}^\varepsilon(\mathbf{x}, t),\ \Psi^\varepsilon(\mathbf{x}, t)\right)$ by the numerical solution of (1.11) in a very fine mesh. It should be emphasized that this step is not necessary in practical applications. Simulations are performed by using the parallel adaptive finite element toolbox PHG on the Lenovo SD530, Xeon Gold 6140 18C/2.3GHz cluster platform. The computational costs for Case 4.1.1 are listed in Table 4.1 and 4.2,

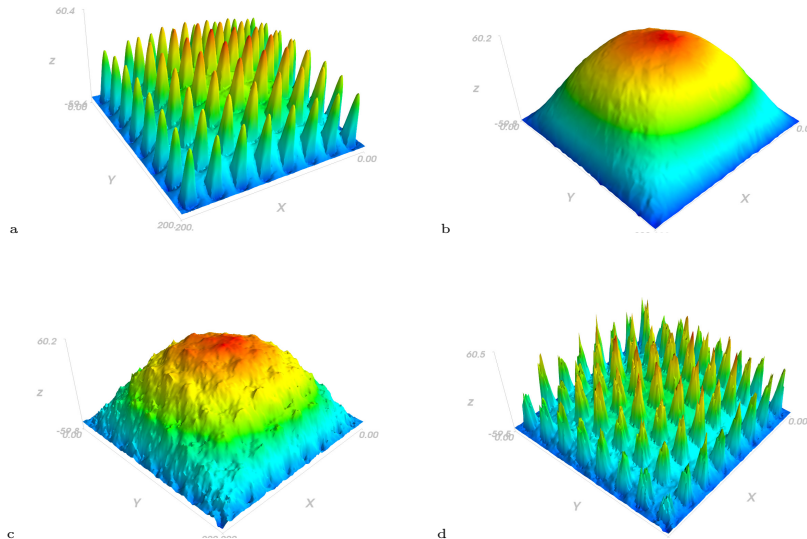which show the advantage of the multiscale numerical method.

FIG. 4.3. *The x_3 component of the vector potential* **A** *on the intersection $x_3 = 0.4$ at time $t = 0.3$ in Case 4.1.2: (a) Reference solution* $\mathbf{A}_3^\varepsilon$ *in fine mesh; (b) homogenization solution* $\mathbf{A}_3^0$ *in coarse mesh; (c) first-order multiscale solution* $\mathbf{A}_3^{\varepsilon,1}$; *(d) second-order multiscale solution* $\mathbf{A}_3^{\varepsilon,2}$.

Without confusion we let $n^\varepsilon = |\Psi^\varepsilon|^2$ and $\mathbf{A}^\varepsilon$ respectively denote the numerical solutions of the density function and the vector potential for the Maxwell–Schrödinger system (1.11) in a fine mesh and regard them as the reference solutions for (1.11). $n^0 = |\Psi^0|^2$ and $\mathbf{A}^0$ are the numerical solutions of the density function and the vector potential for the homogenized Maxwell–Schrödinger system (2.10), respectively. Let $n^{\varepsilon,1} = |\Psi^{\varepsilon,1}|^2$ and $n^{\varepsilon,2} = |\Psi^{\varepsilon,2}|^2$ respectively denote the first-order and the second-order multiscale approximate solutions for the density function based on (2.12)–(2.13). Similarly, Let $\mathbf{A}^{\varepsilon,1}$ and $\mathbf{A}^{\varepsilon,2}$ respectively denote the numerical solutions of the first-order and the second-order multiscale approximate solutions for the vector potential based on (2.12)–(2.13). $\tilde{\mathbf{A}}^{\varepsilon,1}$ and $\tilde{\mathbf{A}}^{\varepsilon,2}$ are respectively the modified first-order and second-order multiscale approximate solutions for the vector potential based on (2.15). Set $e_0 = n^\varepsilon - n^0$, $e_1 = n^\varepsilon - n^{\varepsilon,1}$, $e_2 = n^\varepsilon - n^{\varepsilon,2}$, $\mathbf{e}_0 = \mathbf{A}^\varepsilon - \mathbf{A}^0$, $\mathbf{e}_1 = \mathbf{A}^\varepsilon - \mathbf{A}^{\varepsilon,1}$, $\mathbf{e}_2 = \mathbf{A}^\varepsilon - \mathbf{A}^{\varepsilon,2}$, $\tilde{\mathbf{e}}_1 = \mathbf{A}^\varepsilon - \tilde{\mathbf{A}}^{\varepsilon,1}$, $\tilde{\mathbf{e}}_2 = \mathbf{A}^\varepsilon - \tilde{\mathbf{A}}^{\varepsilon,2}$. For convenience, we use $\|n\|_0$, $\|n\|_1$, $\|\mathbf{A}\|_0$, and $\|\mathbf{A}\|_1$ to denote the numerical approximations of $\|n\|_{L^2(0,T;L^2(\Omega))}$, $\|n\|_{L^2(0,T;H^1(\Omega))}$, $\|\mathbf{A}\|_{L^2(0,T;\mathbf{L}^2(\Omega))}$, and $\|\mathbf{A}\|_{L^2(0,T;\mathbf{H}(\mathbf{curl};\Omega))}$, respectively.

The computational results of the relative errors for Example 4.1 are illustrated in Tables 4.3 and 4.4.

Figures 4.2 (a)–(d) display the numerical results for the density function n^ε, n^0, $n^{\varepsilon,1}$, and $n^{\varepsilon,2}$ on the intersection $x_3 = 0.4$ at time $t = 0.3$ in Case 4.1.1.

Figures 4.3 (a)–(d) display the numerical results for the vector potential $\mathbf{A}^\varepsilon$, $\mathbf{A}^0$, $\mathbf{A}^{\varepsilon,1}$, and $\mathbf{A}^{\varepsilon,2}$ on the intersection $x_3 = 0.4$ at time $t = 0.3$ in Case 4.1.2.

Figures 4.4 (a)–(c) show the numerical results for the vector potential $\mathbf{A}^\varepsilon$, $\mathbf{A}^0$, $\mathbf{A}^{\varepsilon,1}$, and $\mathbf{A}^{\varepsilon,2}$ on the line $x_1 = x_2 = x_3$ at time $t = 0.4$ in Cases 4.1.1 and 4.1.2.
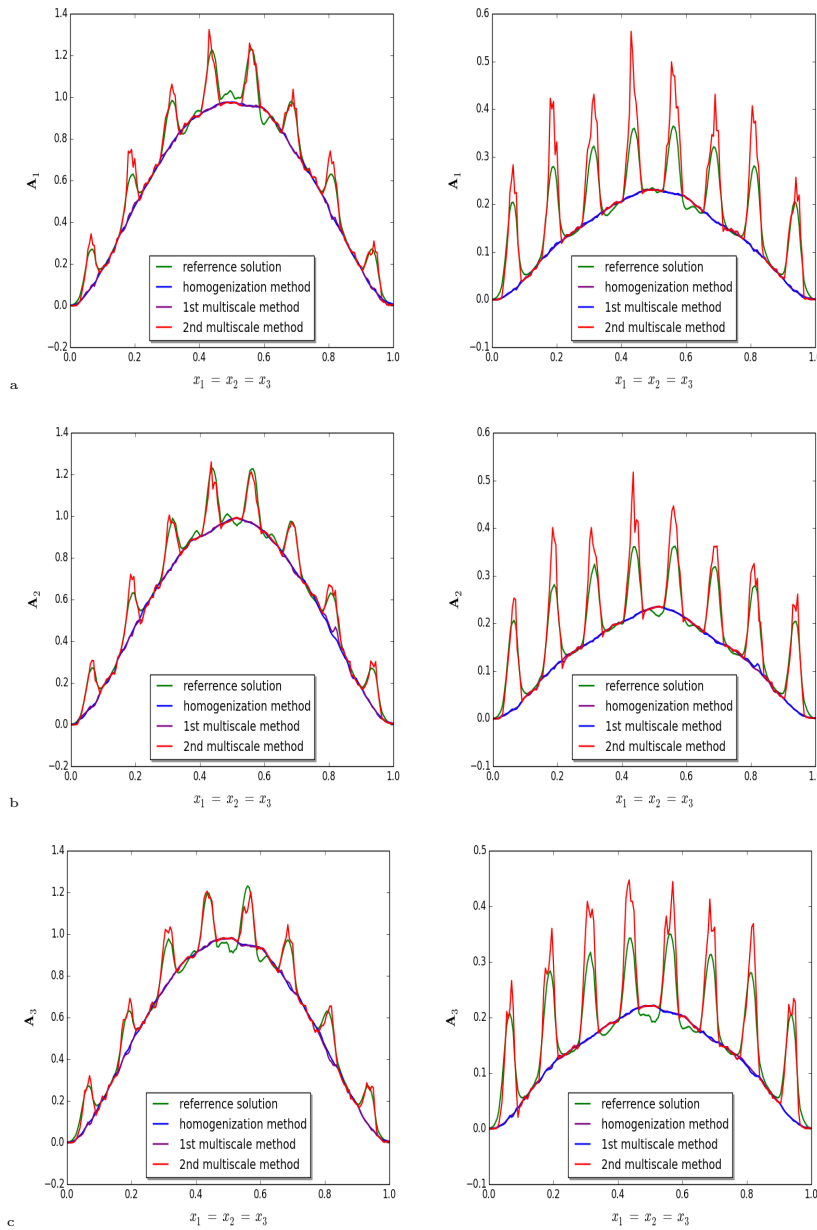
FIG. 4.4. *The multiscale approximate solutions of the vector potential* $\mathbf{A}^\varepsilon$ *on the line* $x_1 = x_2 = x_3$ *at time* $t = 0.4$ *in Case 4.1.1 (left) and Case 4.1.2 (right):* (a) x_1 *component;* (b) x_2 *component;* (c) x_3 *component.*

Remark 4.2. Computational results displayed in Figures 4.2 and 4.3 clearly show that the homogenization method and the first-order multiscale method fail to capture the oscillations of the solutions caused by the rapidly oscillating coefficients matrix. The second-order multiscale solutions are in much better agreement with the reference solutions.

Remark 4.3. In Figure 4.4, we can see that the oscillations of the vector potential $\mathbf{A}^\varepsilon$, i.e., the eight "crests" in the figures, mainly arise from the rapidly oscillating coefficients matrix $B(\frac{\mathbf{x}}{\varepsilon})$. The oscillations caused by the quantum current density between the eight "crests" are negligible. In this example, the (traditional) multiscale asymptotic method is able to produce satisfactory results.
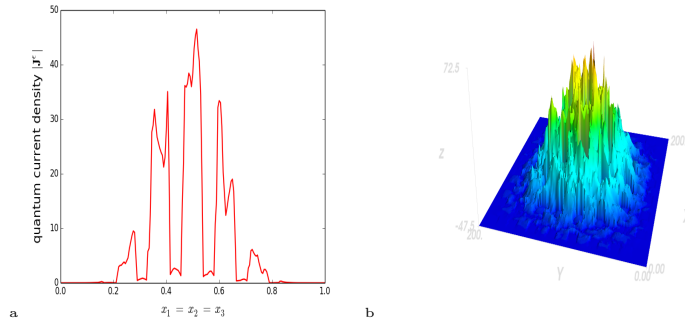

FIG. 4.5. (a) *Case 4.2.1: The quantum current density* $|\mathbf{J}^\varepsilon|$ *on the line* $x_1 = x_2 = x_3$ *at time* $t = 0.25$. (b) *Case 4.2.2: The* x_1 *component of the quantum current density* $\mathbf{J}^\varepsilon$ *on the intersection* $x_3 = 0.4$ *at time* $t = 0.25$.

Example 4.2. In this example, we consider the Maxwell–Schrödinger system (1.11) with the number of electrons $N = 5$. We consider the following cases:

Case 4.2.1. $h_{ij}\left(\dfrac{\mathbf{x}}{\varepsilon}\right) = \begin{cases} 0.025\delta_{ij} & \text{in each dot,} \\ \delta_{ij} & \text{else,} \end{cases} \qquad b_{ij}\left(\dfrac{\mathbf{x}}{\varepsilon}\right) = \begin{cases} \delta_{ij} & \text{in each dot,} \\ 100\delta_{ij} & \text{else,} \end{cases}$

Case 4.2.2. $h_{ij}\left(\dfrac{\mathbf{x}}{\varepsilon}\right) = \begin{cases} 0.025\delta_{ij} & \text{in each dot,} \\ \delta_{ij} & \text{else,} \end{cases} \qquad b_{ij}\left(\dfrac{\mathbf{x}}{\varepsilon}\right) = \begin{cases} \delta_{ij} & \text{in each dot,} \\ 400\delta_{ij} & \text{else.} \end{cases}$

The other computational settings are the same as those in Example 4.1.

Figures 4.5 (a)–(b) display the numerical results for the quantum current density $\mathbf{J}^\varepsilon$ at time $t = 0.25$ in Cases 4.2.1 and 4.2.2.

Figures 4.6 and 4.7 compare the numerical results for the vector potential $\mathbf{A}^\varepsilon$ based on the (traditional) second-order multiscale method and the modified second-order multiscale method at time $t = 0.4$ on the line $x_1 = x_2 = x_3$ in Cases 4.2.1 and 4.2.2.

From Figures 4.5–4.7, we can see that the region where the vector potential $\mathbf{A}^\varepsilon$ is affected greatly by the quantum current density $\mathbf{J}^\varepsilon$ lies at the heart of the domain, where $\mathbf{J}^\varepsilon$ oscillates rapidly.

Remark 4.4. In this example, we can see that the oscillations of the vector potential $\mathbf{A}^\varepsilon$ caused by the quantum current density $\mathbf{J}^\varepsilon$ are more considerable in this example than in Example 4.1 by comparing Figures 4.6 and 4.7 to Figure 4.4. In Case 4.2.1, the oscillations of $\mathbf{A}^\varepsilon$ caused by $\mathbf{J}^\varepsilon$ at the heart of the domain are comparable to those caused by the rapidly oscillating coefficients matrix $B(\frac{\mathbf{x}}{\varepsilon})$. From the numerical results displayed in Figures 4.6 and 4.7, it is easy to see that the modified multiscale method is more capable of capturing the oscillations of $\mathbf{A}^\varepsilon$ caused by $\mathbf{J}^\varepsilon$ than the (traditional) multiscale method.
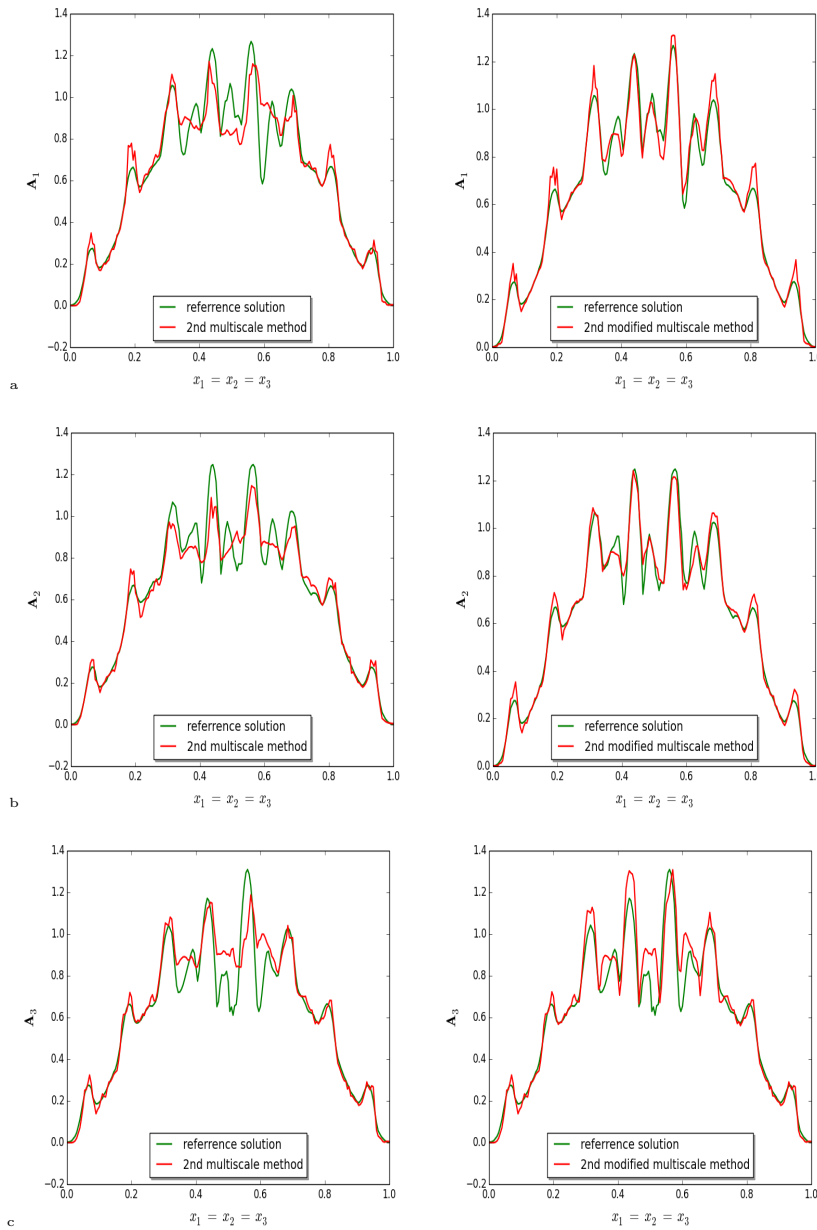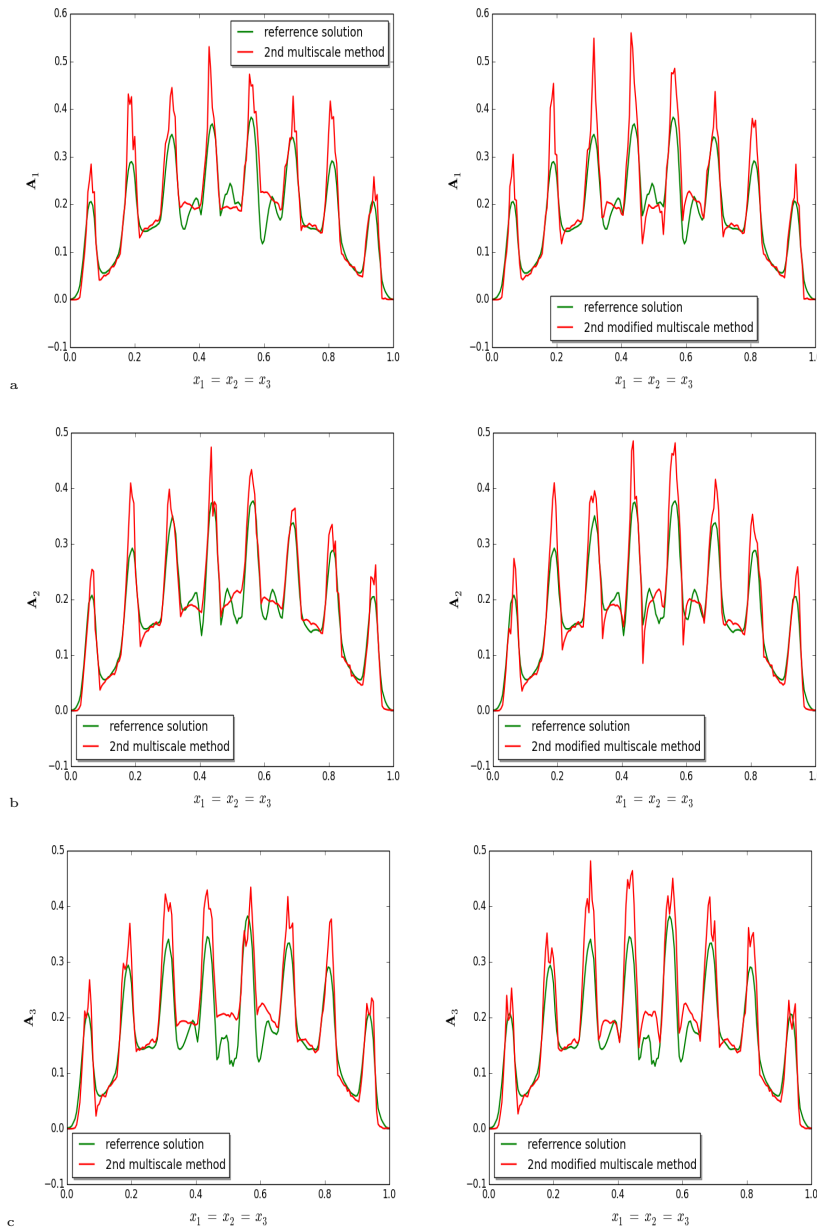
FIG. 4.6. *The second-order multiscale solutions of the vector potential* $\mathbf{A}^\varepsilon$ *at time* $t = 0.4$ *on the line* $x_1 = x_2 = x_3$ *by the (traditional) multiscale method (left) and the modified multiscale method (right) in Case 4.2.1: (a) x_1 component; (b) x_2 component; (c) x_3 component.*

Example 4.3. In this example, we consider the Maxwell–Schrödinger system (1.11) with the exchange-correlation potential and anisotropic coefficients. We take $V_{xc}(\rho) = -\frac{3}{2}\left(\frac{3}{4\pi}\rho\right)^{\frac{1}{3}}$. $\mathbf{J}_s$ and $B(\frac{\mathbf{X}}{\varepsilon})$ are respectively given by

$$\mathbf{J}_s(\mathbf{x}, t) = 1000\big(1 - \cos(\pi t)\big)\big(x_1^2 + 1, \, x_2^2 + 1, \, x_3^2 + 1\big)$$

Fig. 4.7. *The second-order multiscale solutions of the vector potential $\mathbf{A}^\varepsilon$ at time $t = 0.4$ on the line $x_1 = x_2 = x_3$ by the (traditional) multiscale method (left) and the modified multiscale method (right) in Case 4.2.2: (a) x_1 component; (b) x_2 component; (c) x_3 component.*

and

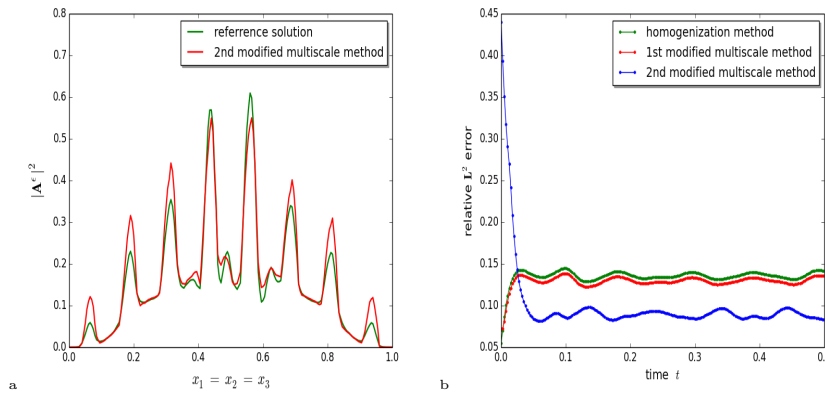$$(4.1) \quad B\left(\frac{\mathbf{x}}{\varepsilon}\right) = \begin{bmatrix} 1 & 0 & 0 \\ 0 & 2 & 0 \\ 0 & 0 & 3 \end{bmatrix} \text{ in each dot;} \quad B\left(\frac{\mathbf{x}}{\varepsilon}\right) = \begin{bmatrix} 200 & 0 & 0 \\ 0 & 400 & 0 \\ 0 & 0 & 300 \end{bmatrix} \text{ else.}$$

FIG. 4.8. *Case 4.3.1:* (a) *The numerical results for* $|\mathbf{A}^\varepsilon|^2$ *at time* $t = 0.5$ *on the line* $x_1 = x_2 = x_3$. (b) *The relative numerical errors of the different methods for* $\mathbf{A}^\varepsilon$ *in* $\mathbf{L}^2(\Omega)$*-norm.*
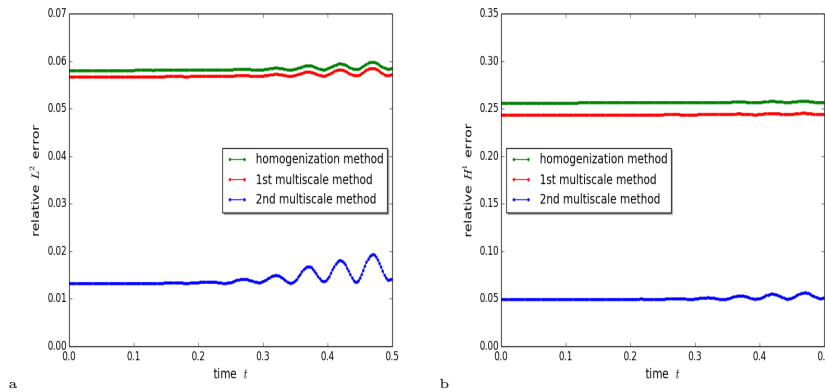

FIG. 4.9. *Case 4.3.2: The relative numerical errors of the different methods for* n^ε *as functions of time in* $L^2(\Omega)$*-norm* (a) *and* $H^1(\Omega)$*-norm* (b).

For the coefficient matrix $H(\frac{\mathbf{x}}{\varepsilon})$, we consider the following cases:

$$
\begin{aligned}
&\text{Case 4.3.1.}\quad && H(\tfrac{\mathbf{x}}{\varepsilon}) = 0.02 \times \widetilde{H} \;\; \text{in each dot;} \quad && H(\tfrac{\mathbf{x}}{\varepsilon}) = \widetilde{H} \;\; \text{else,} \\
&\text{Case 4.3.2.}\quad && H(\tfrac{\mathbf{x}}{\varepsilon}) = 0.02 \times \check{H} \;\; \text{in each dot;} \quad && H(\tfrac{\mathbf{x}}{\varepsilon}) = \check{H} \;\; \text{else,}
\end{aligned}
$$
(4.2)

where

$$
\widetilde{H} = \begin{bmatrix} 1 & 0 & 0 \\ 0 & 2 & 0 \\ 0 & 0 & 3 \end{bmatrix}, \quad \check{H} = \begin{bmatrix} 2 & -1 & 0 \\ -1 & 2 & -1 \\ 0 & -1 & 2 \end{bmatrix}.
$$

The other computational settings are the same as those in Example 4.2. The vector potential is computed by using the modified multiscale method.

Figures 4.8 (a)–(b) show the numerical results for the vector potential $\mathbf{A}^\varepsilon$ in Case 4.3.1. Here, (a) displays the numerical results for $|\mathbf{A}^{\varepsilon}|^2$ based on the modified second-order multiscale method at time $t = 0.5$ on the line $x_1 = x_2 = x_3$, and (b)

displays the relative numerical errors of the homogenization method, the modified first-order multiscale method, and the modified second-order multiscale method for $\mathbf{A}^\varepsilon$ as functions of time in the $\mathbf{L}^2(\Omega)$-norm.

Figures 4.9 (a)–(b) show the relative numerical errors of the homogenization method, the first-order multiscale method, and the second-order multiscale method for the density function n^ε as functions of time in the $L^2(\Omega)$-norm and $H^1(\Omega)$-norm in Case 4.3.2.

Figures 4.10 (a)–(d) display the numerical results for the density function n^ε based on the second-order multiscale method on the intersection $x_3 = 0.6$ at time $t = 0.4$ in Cases 4.3.1 and 4.3.2.
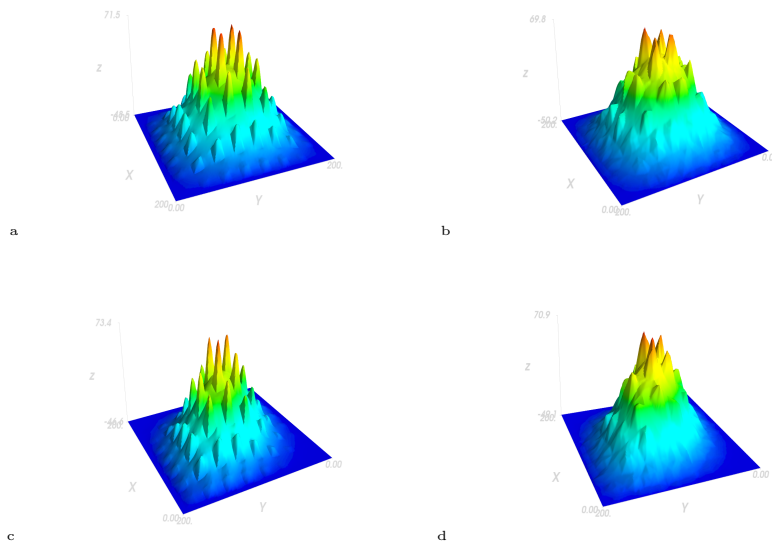

FIG. 4.10. *The density function on the intersection $x_3 = 0.6$ at time $t = 0.4$. (a) Reference solution n^ε in Case* 4.3.1. *(b) Second-order multiscale solution $n^{\varepsilon,2}$ in Case* 4.3.1. *(c) Reference solution n^ε in Case* 4.3.2. *(d) Second-order multiscale solution $n^{\varepsilon,2}$ in Case* 4.3.2.

Example 4.4. To test the convergence performance of the fully discrete finite element scheme (3.9), we consider an artificial problem,

(4.3)
$$
\begin{cases}
-\mathrm{i}\dfrac{\partial \Psi}{\partial t} - (\nabla - \mathrm{i}\mathbf{A})\big(\hat{H}\,(\nabla - \mathrm{i}\mathbf{A})\Psi\big) + \big(\langle V_c \rangle + V_{xc}[N|\Psi|^2]\big)\Psi = g \quad \text{in } \Omega \times (0,T), \\[2mm]
\dfrac{\partial^2 \mathbf{A}}{\partial t^2} + \nabla \times (\hat{B}\,\nabla \times \mathbf{A}) - 2N\hat{H}\,\mathrm{Im}\big[(\Psi)^*(\nabla - \mathrm{i}\mathbf{A})\Psi\big] = \mathbf{f} \quad \text{in } \Omega \times (0,T), \\[2mm]
\Psi(\mathbf{x},t) = 0, \quad \mathbf{A}(\mathbf{x},t) \times \mathbf{n} = 0, \quad (\mathbf{x},t) \in \partial\Omega \times (0,T), \\[2mm]
\Psi(\mathbf{x},0) = \Psi_0(\mathbf{x}), \quad \mathbf{A}(\mathbf{x},0) = \mathbf{A}_0(\mathbf{x}), \quad \mathbf{A}_t(\mathbf{x},0) = \mathbf{A}_1(\mathbf{x}) \text{ in } \Omega,
\end{cases}
$$

where $\Omega = (0,1)^3$, $T = 3.0$, and $N = 1$. We take $\langle V_c \rangle = 5.0$ and $V_{xc}(s) = \frac{1}{2}s^2$. The
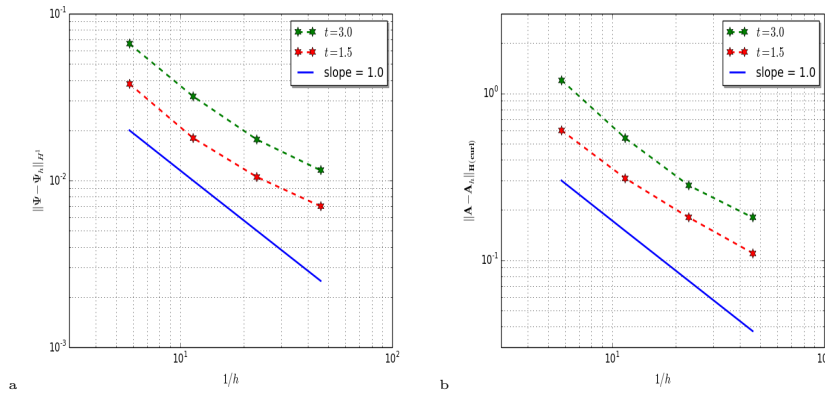
FIG. 4.11. *The errors at $t = 1.5$ and $t = 3.0$. (a) The error of the wave function Ψ in H^1-norm.* (b) *The error of the vector potential $\mathbf{A}$ in $\mathbf{H}(\mathbf{curl})$-norm.*
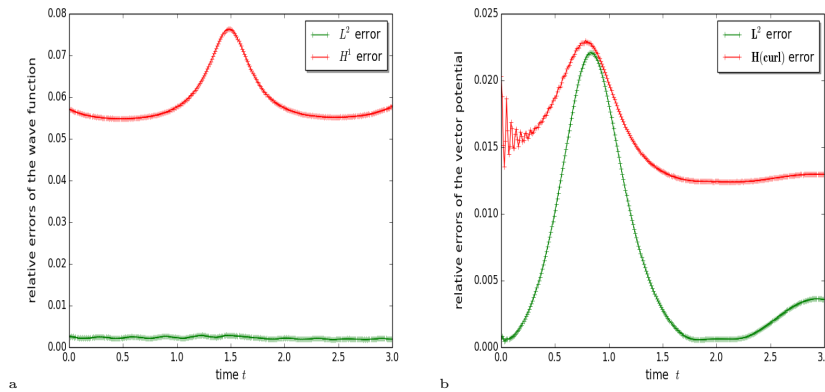

FIG. 4.12. *The relative errors of the wave function Ψ in L^2-norm and H^1-norm* (a) *and the vector potential $\mathbf{A}$ in $\mathbf{L}^2$-norm and $\mathbf{H}(\mathbf{curl})$-norm* (b). $h = 0.043$; $\tau = 0.01$.

matrices $\hat{H}$ and $\hat{B}$ are given by

$$\hat{H} = \begin{bmatrix} 2 & -1 & 0 \\ -1 & 2 & -1 \\ 0 & -1 & 2 \end{bmatrix}, \quad \hat{B} = \begin{bmatrix} 2 & 2 & 0 \\ 2 & 5 & 3 \\ 0 & 3 & 9 \end{bmatrix}.$$

The functions g, $\mathbf{f}$, Ψ_0, $\mathbf{A}_0$, and $\mathbf{A}_1$ are chosen corresponding to the exact solution

$$\Psi(\mathbf{x}, t) = \left(e^{i\pi t} + 2i\right) x_1 x_2 x_3 (1 - x_1)(1 - x_2)(1 - x_3),$$
$$\mathbf{A}(\mathbf{x}, t) = \left(\cos(\pi t) + 2t\right)\left(\sin(\pi x_2)\sin(\pi x_3), \ \sin(\pi x_1)\sin(\pi x_3), \ \sin(\pi x_1)\sin(\pi x_2)\right).$$

In Figure 4.11, we plot the errors at $t = 1.5$ and $t = 3.0$ for a sequence of successively refined tetrahedral meshes starting from a uniform coarse mesh. The initial mesh is obtained by a uniform subdivision of a finite difference grid of the domain Ω. We take a sufficiently small time-step τ such that the errors are mainly due to spatial discretization. The errors are displayed in logarithmic scale as a function of $1/h$, which

allows us to visualize the convergence rates as the slopes of the curves. We observe that the convergence orders are slightly smaller than 1 as the mesh is successively refined.

In Figure 4.12, we display the relative errors as functions of time in which the system is solved with $\tau = 0.01$ and $h = 0.043$. The mesh used in this case consists of 384000 tetrahedrons.

5. Conclusions. We have developed the homogenization and multiscale asymptotic method for the Maxwell–Schrödinger system under the temporal gauge with the rapidly oscillating effective mass and magnetic permeability. A novel multiscale approximation is proposed for the vector potential to capture the oscillations caused by the quantum current density. In addition, we propose a Crank–Nicolson finite element method for the homogenized Maxwell–Schödinger system and establish the stability estimates. Numerical examples are presented to show the efficiency and accuracy of the algorithms. For now, some aspects of the algorithms proposed in this paper have not been touched upon yet, including the following:

1. The homogenization and multiscale asymptotic method for the Maxwell–Schrödinger system in which the heterogeneity in the electric permittivity and the magnetic permeability are both considered.
2. A rigorous proof of the convergence of the homogenization method for the Maxwell–Schrödinger system.
3. Theoretical analysis of the modified multiscale approximation for the vector potential.
4. Theoretical analysis of the error introduced by replacing the homogenized matrices $\hat{H}$ and $\hat{B}$ in the system (3.9) with the approximations $\hat{H}^{h_0}$ and $\hat{B}^{h_0}$, respectively.
5. A rigorous proof of the convergence of the Crank–Nicolson finite element method for the homogenized Maxwell–Schrödinger system.

Building on the work in this paper, in the near future we plan to investigate the theoretical analysis of the modified multiscale approximation and the Crank–Nicolson finite element method for the homogenized Maxwell–Schrödinger system. Moreover, from the point of view of practical applications, extending the present results to the Maxwell–Schrödinger system with the rapidly oscillating electric permittivity is another focus of future work.

REFERENCES

[1] I. AHMED AND E. LI, *Simulation of plasmonics nanodevices with coupled Maxwell and Schrödinger equations using the FDTD method*, Adv. Electromagnetics, 1 (2012), pp. 76–83.
[2] G. ALLAIRE AND A. PIATNITSKI, *Homogenization of the Schrödinger equation and effective mass theorems*, Communications in Mathematical Physics, 258 (2005), pp. 1–22.
[3] G. BAO, D. LIU, AND S. LUO, *Multiscale modeling and computation of optically manipulated nano devices*, J. Comput. Phys., 316 (2016), pp. 558–572.
[4] A. BENSOUSSAN, J. LIONS, AND G. PAPANICOLAOU, *Asymptotic Analysis for Periodic Structures*, North-Holland, Amsterdam, 1978.
[5] S. BRENNER AND L. SCOTT, *The Mathematical Theory of Finite Element Methods*, Springer, New York, 2002.
[6] L. Q. CAO, Y. ZHANG, W. ALLEGRETTO, AND Y. P. LIN, *Multiscale asymptotic method for Maxwell's equations in composite materials*, SIAM J. Numer. Anal., 47 (2010), pp. 4257–4289, https://doi.org/10.1137/080741276.

[7] L. Q. Cao, K. Q. Li, J. L. Luo, and Y. S. Wong, *A multiscale approach and a hybrid FE-FDTD algorithm for 3D time-dependent Maxwell's equations in composite materials*, Multiscale Model. Simul., 13 (2015), pp. 1446–1477, https://doi.org/10.1137/140999694.

[8] L. Q. Cao, J. L. Luo, and C. Y. Wang, *Multiscale analysis and numerical algorithm for the Schrödinger equations in heterogeneous media*, Appl. Math. Comput., 217 (2010), pp. 3955–3973.

[9] W. C. Chew, *Vector potential electromagnetics with generalized gauge for inhomogeneous media: Formulation*, Progr. Electromagn. Res., 149 (2014), pp. 69–84.

[10] Q. Chen, H. Qin, J. Liu, J. Xiao, R. Zhang, Y. He, and Y. Wang, *Canonical symplectic structure and structure-preserving geometric algorithms for Schrödinger–Maxwell systems*, J. Comput. Phys., 349 (2017), pp. 441–452.

[11] Y. P. Chen, W. E, I. Sha, L. J. Jiang, M. Meng, Y. M. Wu, and W. C. Chew, *A unified Hamiltonian solution to Maxwell–Schrödinger equations for modelling electromagnetic field-particle interaction*, Comput. Phys. Comm., 215 (2017), pp. 63–70.

[12] D. Cioranescu and P. Donato, *An Introduction to Homogenization*, Oxford University Press, New York, 1999.

[13] M. Delfour, M. Fortin, and G. Payne, *Finite difference solution of a nonlinear Schrödinger equation*, J. Comput. Phys., 44 (1981), pp. 277–288.

[14] Y. Fu, *Physical Models of Semiconductor Quantum Devices*, Springer, New York, 2014.

[15] D. A. Genov, A. K. Sarychev, V. M. Shalaev, and A. Wei, *Resonant field enhancements from metal nanoparticle arrays*, Nano Lett., 4 (2004), pp. 153–158.

[16] W. Greiner and D. A. Bromley, *Quantum Mechanics. An introduction*, 4th ed., Springer, New York, 2000.

[17] G. Leoni, *A First Course in Sobolev Spaces*, 2nd ed., Carnegie Mellon University, Pittsburgh, PA, 2017.

[18] E. Lorin, S. Chelkowski, and A. D. Bandrauk, *A numerical Maxwell–Schrödinger model for intense laser–matter interaction and propagation*, Comput. Phys. Comm., 177 (2007), pp. 908–932.

[19] X. Z. Liu, T. Galfsky, Z. Sun, F. Xia, E.-C. Lin, Y.-H. Lee, S. Kéna-Cohen, and V. M. Menon, *Strong light-matter coupling in two-dimensional atomic crystals*, Nature Photonics, 9 (2015), pp. 30–34.

[20] E. H. Lieb and M. Loss, *Analysis*, 2nd ed., AMS, Providence, RI, 2001.

[21] C. P. Ma, L. Q. Cao, and Y. P. Lin, *Error estimates of the Crank–Nicolson Galerkin method for the time-dependent Maxwell–Schrödinger equations under the Lorentz gauge*, IMA J. Numer. Anal., 38 (2018), pp. 2074–2104.

[22] C. P. Ma, L. Q. Cao, and J. Z. Huang, *Analysis of a fully discrete finite element method for the Maxwell–Schrödinger system in the Coulomb gauge*, Internat. J. Numer. Anal. Model., 16 (2019), pp. 139–166.

[23] P.Monk, *Finite Element Methods for Maxwell's Equations*, Clarendon Press, Oxford, UK, 2003.

[24] L. Pierantoni, D. Mencarelli, and T. Rozzi, *A new 3-D transmission line matrix scheme for the combined Schrödinger–Maxwell problem in the electronic/electromagnetic characterization of nanodevices*, IEEE Trans. Microwave Theory Tech., 56 (2008), pp. 654–662.

[25] C. J. Ryu, A. Y. Liu, W. E. I. Wei, and W. C. Chew, *Finite-difference time-domain simulation of the Maxwell–Schrödinger system*, IEEE J. Multiscale Multiphys. Comput. Tech., 1 (2016), pp. 40–47.

[26] L. Signing, *Periodic homogenization of Schrödinger type equations with rapidly oscillating potential*, Afr. Diaspora J. Math., 19 (2016), pp. 29–45.

[27] W. Strauss and L. Vázquez, *Numerical solution of a nonlinear Klein–Gordon equation*, J. Comput. Phys., 28 (1978), pp. 271–278.

[28] Y. Todorov, A. M. Andrews, R. Colombelli, S. De Liberato, C. Ciuti, P. Klang, G. Strasser, and C. Sirtori, *Ultrastrong light-matter coupling regime with polariton dots*, Phys. Rev. Lett., 105 (2010), 196402.

[29] T. C. Wang, B. L. Guo, and Q. B. Xu, *Fourth-order compact and energy conservative difference schemes for the nonlinear Schrödinger equation in two dimensions*, J. Comput. Phys., 243 (2013), pp. 382–399.

[30] N. Wellander, *Homogenization of the Maxwell equations. Case I. Linear theory*, Appl. Math., 46 (2001), pp. 29–51.

[31] N. Wellander, *Homogenization of the Maxwell equations. Case II. Nonlinear conductivity*, Appl. Math., 47 (2002), pp. 255–283.

[32] C. Xiang, F. M. Kong, K. Li, and M. Liu, *A high-order symplectic FDTD scheme for the Maxwell–Schrödinger system*, IEEE J. Quantum Electron., 54 (2018), pp. 1–8.

[33] C. Y. Yam, L. Y. Meng, Y. Zhang, and G. H. Chen, *A multiscale quantum mechanics/electromagnetics method for device simulations*, Chem. Soc. Rev., 44 (2015), pp. 1763–1776.

[34] L. Zhang, L. Q. Cao, and J. L. Luo, *Multiscale analysis and computation for a stationary Schrödinger–Poisson system in heterogeneous nanostructures*, Multiscale Model. Simul., 12 (2014), pp. 1561–1591, https://doi.org/10.1137/13091991X.

[35] Y. Zhang, L. Q. Cao, and Y. S. Wong, *Multiscale computations for 3D time-dependent Maxwell's equations in composite materials*, SIAM J. Sci. Comput., 32 (2010), pp. 2560–2583, https://doi.org/10.1137/080740337.